

# A grain level model for the study of failure initiation and evolution in polycrystalline brittle materials. Part II: Numerical examples

Horacio D. Espinosa <sup>\*</sup>, Pablo D. Zavattieri <sup>1</sup>

*Department of Mechanical Engineering, Northwestern University, 2145 Sheridan Road, Evanston, IL 60208-3111, USA*

Received 17 September 2001; received in revised form 11 April 2002

---

## Abstract

Numerical aspects of the grain level micromechanical model presented in part I are discussed in this study. They include, an examination of solution convergence in the context of cohesive elements used as an approach to model crack initiation and propagation; performance of parametric studies to assess the role of grain boundary strength and toughness, and their stochasticity, on damage initiation and evolution. Simulations of wave propagation experiments, performed on alumina, are used to illustrate the capabilities of the model in the framework of experimental measurements. The solution convergence studies show that when the length of the cohesive elements is smaller than the cohesive zone size and when the initial slope of the traction-separation cohesive law is properly chosen, the predictions concerning microcrack initiation and evolution are mesh independent. Other features examined in the simulations were the effect of initial stresses and defects resulting from the material manufacturing process. Also described are conditions on the selection of the representative volume element size, as a function of ceramic properties, to capture the proper distance between crack initiation sites. Crack branching is predicted in the case of strong ceramics and sufficient distance between nucleation sites. Rate effects in the extension of microcracks were studied in the context of damage kinetics and fragmentation patterns. The simulations show that crack speed can be significantly varied in the presence of rate effects and as a result crack diffusion by nucleation of multiple sites achieved. This paper illustrates the utilization of grain level models to predict material constitutive behavior in the presence, or absence, of initial defects resulting from material manufacturing. Likewise, these models can be employed in the design of novel heterogeneous materials with hierarchical microstructures, multi-phases and/or layers.

© 2002 Elsevier Science Ltd. All rights reserved.

---

<sup>\*</sup>Corresponding author. Tel.: +847-467-5989; fax: +847-491-3915.

E-mail address: [espinosa@northwestern.edu](mailto:espinosa@northwestern.edu) (H.D. Espinosa).

URL: <http://www.mech.northwestern.edu/espinosa>.

<sup>1</sup> Present address: General Motors Research and Development Center, 30500 Mound Road, Warren, MI 48090-9055, USA.

## 1. Introduction

The grain level micromechanical model presented in part I is used to analyze the evolution of damage in ceramics when they are subjected to stress pulses that are large enough in amplitude to initiate microcracks, but short enough in duration

to prevent their coalescence into macrocracks. Since failure processes in ceramics are transient in nature, even under nominally quasi-static loading conditions, inertia effects play an important role. Normal plate impact experiments have proved to be successful in inducing microcracking in alumina under well-known and controlled loading conditions without causing macroscopic failure of the material (Raiser et al., 1990, 1994; Raiser, 1993; Espinosa, 1992; Espinosa et al., 1992). This experiment uses an eight pointed star-shaped flyer plate that impacts a square ceramic specimen, subjecting the central octagonal region to a plane pulse. Fig. 1 shows the soft-recovery normal impact configuration. A tensile pulse is originated, from an intentional gap manufactured between the specimen and the momentum trap, upon reflection of the compressive pulse.

A detailed study of the damage kinetics in these experiments was recently carried out by Zavattieri and Espinosa (2001). The interferometrically

measured velocity profiles obtained from these experiments, which are very rich in information concerning damage initiation and kinetics as well as postmortem SEM and TEM observations, make this experiment an ideal candidate for the analysis of material failure in conjunction with the proposed grain level micromechanical model under a fully dynamic framework. The experiments and simulations not only allow identification of model parameters but also explain the different failure mechanisms of ceramics as a function of microstructure morphology and grain boundary chemistry.

Analyzing the time history of failure is more important than simply examining the final outcome. While postmortem observations can reveal failure mechanisms such as inter-granular and transgranular fractures and their relative proportions, they do not indicate the sequential order of the events or the conditions for crack initiation. Additionally, postmortem observations do not provide sufficient information about microfracture nor evolution of stress-carrying capacity.

The focus of this contribution is in the numerical aspects of the proposed grain level micromechanical model. To illustrate the capabilities of the model, the normal impact experiments performed on  $\text{Al}_2\text{O}_3$  by Raiser et al. (1990) and Espinosa (1992) are studied while focusing on the effects of interface element parameters, grain anisotropy, grain size, and stochastic distribution of grain boundary properties. The paper starts with the definition of computational cell, boundary and initial conditions. A section is devoted to the analysis of solution convergence in the context of cohesive elements as an approach to model crack initiation and propagation. A parametric analysis is conducted to examine the effect of representative volume element (RVE) size and cohesive element properties on damage evolution. The effect of initial microcracks, resulting from the sintering process, grain boundary strength, and rate dependent microcracking are investigated in various subsections. The effect of crack initiation distance on propagation and branching is also examined in ceramics with strong grain boundaries, i.e., high purity ceramics.

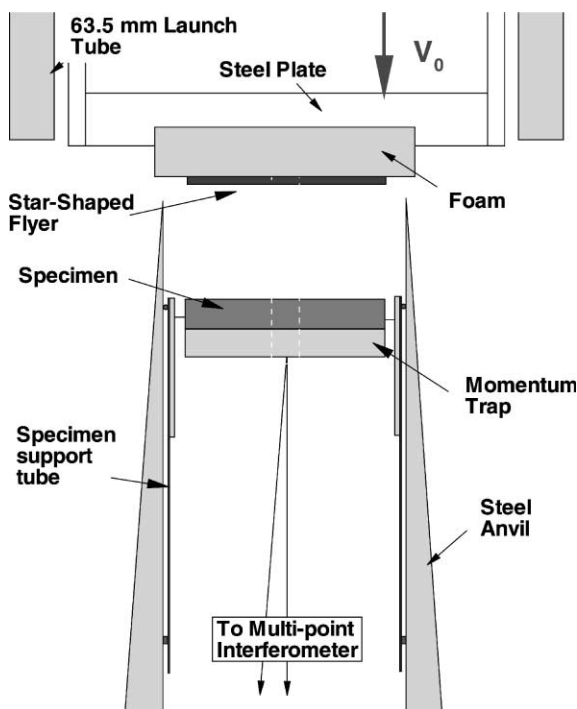


Fig. 1. Soft-recovery normal impact configuration.

## 2. Definition of computational cell

A RVE of an actual microstructure is considered for the analysis. An elastic-anisotropic model for the grains, incorporating grain anisotropy, is used under plane strain conditions. Cohesive interface elements are embedded along grain boundaries to simulate microcrack initiation and evolution. The normal and shear traction components in the interface elements are calculated from the interface cohesive laws presented in part I of this work. The grain morphology is represented by

either digitizing a real ceramic microstructure or automatically generating a Voronoi Tessellation.

In view of the uniaxial strain conditions prevailing in the specimen and assuming periodicity, a RVE of only part of the ceramic specimen is considered. Fig. 2(a) shows a strip of the experimental configuration: flyer, momentum trap, and specimen plates are considered in the analysis. Furthermore, for the low impact velocities considered in these simulations, only a small portion of the ceramic plate, in the spall region, is simulated. The dimensions of the cell are  $L \times H$ . This

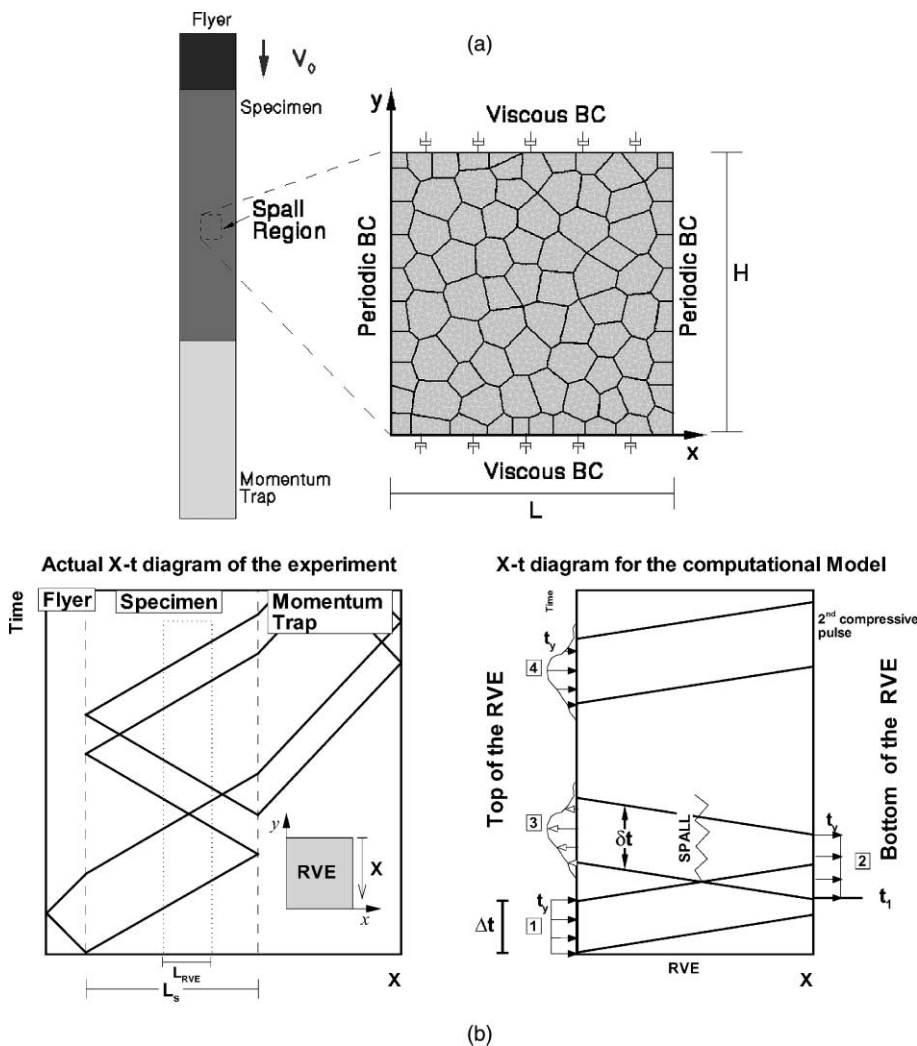


Fig. 2. (a) Schematics of the computational cell used in the analyses. (b) Schematic of boundary conditions employed in the analyses.

feature is consistent with experimental observations showing that damage and inelasticity, at impact velocities below 100 m/s, are restricted to the spall region.

### 3. Boundary and initial conditions

Assuming that the computational cell is repeated in the  $x$ -direction, the following periodic boundary conditions are applied

$$\begin{aligned} \mathbf{u}(0, y, t) &= \mathbf{u}(L, y, t), \quad \mathbf{v}(0, y, t) = \mathbf{v}(L, y, t), \\ \mathbf{a}(0, y, t) &= \mathbf{a}(L, y, t) \end{aligned} \quad (1)$$

where  $L$  is the width of the cell,  $\mathbf{u}$ ,  $\mathbf{v}$  and  $\mathbf{a}$  are the displacement, velocity and acceleration vector fields. Grains with nodes at  $x = 0$  have the same principal material directions as the grains with nodes at  $x = L$  to ensure periodicity. Furthermore, assuming that there is no damage in the ceramic, except in the spall region where it remains elastic throughout the deformation process, the computational effort can be minimized by replacing the rest of the ceramic with viscous boundary conditions based on one dimensional elastic wave theory, as discussed in part I. Conservation of momentum and continuity of velocities and tractions lead to the following equations for traction components  $t_x$  and  $t_y$  at  $y = H$  and  $y = 0$ , namely,

$$t_x(x, H, t) = (\rho c_s)_c v_x(x, H, t) \quad (2)$$

$$t_y(x, H, t) = (\rho c_l)_c [v_y(x, H, t) - 2v_y^1] \quad (3)$$

$$t_x(x, 0, t) = (\rho c_s)_c v_x(x, 0, t) \quad (4)$$

$$t_y(x, 0, t) = (\rho c_l)_c v_y(x, 0, t) \quad (5)$$

where  $(\ )_c$  are ceramic quantities,  $c_l$  and  $c_s$  are longitudinal and shear wave speeds,  $\rho$  is the specific material density,  $v_x$  and  $v_y$  are the transverse and normal velocities at the top of the RVE and  $v_y^1$  is the normal velocity at the flyer-specimen interface, which can be computed from the impact velocity  $V_0$  by

$$v_y^1 = \frac{(\rho c_l)_f}{(\rho c_l)_s + (\rho c_l)_f} V_0 \quad (6)$$

in which  $(\rho c_l)_f$  is longitudinal impedance of the flyer. Here the reference point 1 is at the flyer-specimen interface, and the normal traction on this interface is given by  $t_y^1 = -2(\rho c_l)_c v_y^1$ .

The initial transverse and normal velocities at the bottom of the RVE are set to zero and at the top of the RVE are given by

$$v_x(x, H, 0) = 0 \quad (7)$$

$$v_y(x, H, 0) = v_y^1 \quad (8)$$

As discussed earlier, since the RVE is much smaller than the actual thickness of the ceramic, special care must be taken at the boundaries to include the reflection of the waves from free surfaces and the contact with the momentum trap plate upon closure of the gap. The traction at the top of the RVE, which is given by Eq. (3), is used to simulate the compressive wave generated at the flyer-specimen interface until the unloading of the wave reaches that point. Assuming that there is no damage in compression, the duration of the first compressive pulse can be reduced in the simulations. Fig. 2(b) shows the Lagrangian  $X-t$  diagram corresponding to the wave history, at the boundary of the RVE, for the normal plate impact experiments. In this diagram,  $L_s$  represents the thickness of the specimen and  $L_{RVE}$  represents the height, i.e.,  $H$ , of the RVE considered in the analysis. Since the duration of the first compressive pulse inside the specimen is  $\Delta t$ , the traction is removed at  $t = \Delta t$  to account for the unloading originated at the flyer plate. The compressive traction at the bottom of the RVE is given by Eq. (5). Right after the first compression wave reaches the bottom of the RVE, the unloading from the back of the specimen is represented by new viscous boundary conditions at time  $t_1$ . In order to simulate this wave reflection, the normal traction at  $y = 0$  is modified to include such information. The time at which this traction is applied is  $t_1 = \Delta t$ . In this way, the spall plane is located at the middle of the RVE. The contact with the momentum trap occurs at  $t_1 + \delta t$ , where  $\delta t$  is the duration of the unloading pulse. This second pulse then travels through the RVE and becomes tensile. Since this second pulse is modified by microcracking, the traction at the top of the RVE is *recorded* and

stored so that it can be used to simulate its reflection at the impact surface (see Fig. 2(b) state 4 on the right).

The velocity  $v_y(x, 0, t)$  at the bottom of the RVE can be directly compared with the experimental velocity history if two important features are taken into account:

1. The velocity is corrected according to the impedances of the specimen and momentum trap. The velocity at the specimen-momentum trap interface  $v_y^f$  (after contact) is given by  $v_y^f = 2(\rho c_1)_s v_y(x, 0, t) / ((\rho c_1)_{MT} + (\rho c_1)_s)$ , where  $(\ )_s$  and  $(\ )_{MT}$  denote specimen and momentum trap quantities, respectively. Considering that the velocity at the back of the momentum trap is twice  $v_y^f$ , this correction is given by

$$v_y = \frac{4(\rho c_1)_s}{(\rho c_1)_{MT} + (\rho c_1)_s} v_y(x, 0, t) \quad (9)$$

2. The time at which waves arrive to the back of the momentum trap is different to the one in the simulation due to the simplifications of the model (i.e., the reduction of the duration of the compression wave, etc.). The effect can be taken into account exactly by using pulse durations, longitudinal wave speeds and width of plates and RVE.

The material properties of the ceramic specimen ( $\text{Al}_2\text{O}_3$ ) are given in Table 1. The nonzero components are denoted by only two indices (i.e.,  $C_{1111} = C_{11}$ ,  $C_{2222} = C_{22}$ ,  $C_{1122} = C_{12}$ ,  $C_{1212} = C_{44}$ , etc.). It should be noted that alumina is a trigonal system with only three planes of symmetry with normals that do not coincide with the local axes of co-ordinates except for axis 1. In terms of the

Table 1

Material properties for alumina

Specimen properties: anisotropic elastic constant for alumina $\text{Al}_2\text{O}_3$	$\text{Al}_2\text{O}_3$ (GPa) (Hearmon, 1956)
$C_{11} = C_{22}$	465
$C_{12}$	124
$C_{13} = C_{23}$	117
$C_{14} = -C_{24}$	101
$C_{33}$	563
$C_{44} = \frac{1}{2}(C_{11} - C_{12})$	
$C_{55} = C_{66}$	233

elastic constitutive matrix  $\hat{\mathcal{C}}_{IJ}$ , this means that  $C_{14} = -C_{24} = C_{45} \neq 0$  (Hearmon, 1956). In order to perform plane strain analyses, the behavior of alumina is assumed to be transversely isotropic (or hexagonal) making  $C_{14} = 0$ . Other mechanical material parameters needed for this analysis are wave speeds, impedances and densities of the different materials used in the experiments, which are given in Table 2.

#### 4. Solution convergence analysis

In addition to the usual requirements of mesh independence, two other factors influence the solution convergence of this grain level micromechanical model.

First, the finite element size must be small enough to accurately resolve the stress distribution in the cohesive zone at microcrack tips. For a linearly softening cohesive law, an approximation of the cohesive zone size  $d_{cz}$  at the crack tip is given by Rice (1968) as

$$d_{cz} \approx \frac{\pi}{2} \frac{E}{(1-\nu^2)} \frac{G_{IC}}{T_{\max}^2} = \frac{\pi}{2} \left( \frac{K_{IC}}{T_{\max}} \right)^2 \quad (10)$$

Table 2

Properties of the different materials used in the experiments

Material	Longitudinal wave speed $c_1$ , mm/ $\mu$ s	Transverse wave speed $c_s$ , mm/ $\mu$ s	Acoustic impedance, $\rho c_1$ GPa/mm/ $\mu$ s	Shear impedance, $\rho c_s$ GPa/mm/ $\mu$ s	Mass density, $\rho$ , kg/m <sup>3</sup>
1018 CR	5.9	3.2	45.50	24.70	7700
Hampden	5.9	3.2	47.03	25.66	7861
Al6061-T6	6.4	3.0	17.34	8.23	2700
Ti6Al4V	6.2	3.1	27.71	13.96	4430
$\text{Al}_2\text{O}_3$	10.8	6.4	43.09	25.54	3990

where  $\nu$  is the Poisson's ratio,  $G_{IC}$  and  $K_{IC}$  are the critical energy release rate and the fracture toughness of the material in mode I, respectively. In order to resolve the cohesive zone field, it is necessary for the maximum interface element size,  $h_c$ , inside the cohesive zone, to satisfy the following inequality:

$$h_c \ll d_{cz} \quad (11)$$

The second constraint for solution convergence is related to the initial slope of the cohesive law, see part I of this work. According to the traction-separation relationship, this slope is given as

$$s = \frac{T_{\max}}{\lambda_{cr} \delta} \quad (12)$$

This initial slope works as a penalty parameter. As the parameter grows, the solution improves. Hence, it has to be large enough to be effective but not so large as to provoke numerical instabilities. According to Eq. (42) of part I, the element size must satisfy the following inequality:

$$\lambda_{cr} \ll \frac{Th}{E\delta} \quad (13)$$

where  $h$  is the size of the triangular element. Since we are using two linear interface elements on each edge of the triangular element,  $h = 2h_c$ . For a given element size, the parameter  $\lambda_{cr}$  can be chosen in order to satisfy Eq. (13). However, it should be noted that the critical effective displacement jump cannot exceed unity,  $\lambda_{cr} \leq 1$ ; therefore, the maximum separation  $\delta$  would be limited by the following expression:

$$\delta \geq T_{\max}/s \quad (14)$$

This means that for a given slope and  $T_{\max}$ , the maximum separation and, therefore, the area below the curve, cannot exceed a certain value. Moreover, it is desired that

$$\lambda_{cr} \ll 1 \quad (15)$$

Note that Eq. (13) can also be written in the following way:

$$h \gg \lambda_{cr} \frac{E}{T_{\max}} \delta \quad (16)$$

According to this equation, the higher  $T_{\max}$ , the smaller the element should be unless the critical energy release rate (or  $\delta$ ) is increased.

Typical values of  $d_{cz}$  and  $h$  can be obtained for different  $T_{\max}$ – $K_{IC}$  pairs. For instance, for  $T_{\max} = 1$  GPa and  $K_{IC} = 1$  MPa m<sup>1/2</sup> the cohesive zone is  $d_{cz} = 1.57$   $\mu\text{m}$  and the required element size according to Eq. (16) is  $h_c = h/2 \gg 1.41$   $\mu\text{m}$  for a minimum slope of 200 GPa/ $\mu\text{m}$ . Hence,  $h_c$  must be  $\gg 1.41$  and  $\ll 1.57$   $\mu\text{m}$  according to Eq. (11). It should be noted that the above minimum slope  $s = T_{\max}/\delta$  corresponds to  $\lambda_{cr} = 1$ . In practice, it is desirable to have  $\lambda_{cr} \ll 1$  if the slope and element size are to be optimum. For the previous example, if  $\lambda_{cr} = 0.1$  is considered the minimum slope is  $s = 2000$  GPa/ $\mu\text{m}$  and the required element size is about  $h = 0.14$   $\mu\text{m}$ , which easily satisfies Eq. (11). As previously noticed, the maximum allowable element size becomes smaller for higher values of  $T_{\max}$ . In fact, for  $T_{\max} = 10$  GPa and  $K_{IC} = 2$  MPa m<sup>1/2</sup> the cohesive zone is  $d_{cz} = 0.06$   $\mu\text{m}$  and the required element size is  $h_c = 0.06$   $\mu\text{m}$  for a minimum slope of 5500 GPa/ $\mu\text{m}$  and  $\lambda_{cr} = 0.1$ .

The above analysis shows that elements smaller than 0.1  $\mu\text{m}$  are needed for microstructures with interfacial strength as high as  $T_{\max} = E/40$ . Likewise,  $\lambda_{cr}$  must be selected such that Eq. (13) is also satisfied!

Fig. 3(a) shows the finite element meshes utilized to study the solution convergence for a Voronoi microstructures. In this case, a RVE of  $20 \times 20$   $\mu\text{m}$  with a grain size  $GS = 2$   $\mu\text{m}$ , is generated. The boundary conditions are applied according to the previous section, the impact velocity is  $V_0 = 90$  m/s and the tensile pulse duration is  $\delta t = 40$  ns. Several meshes are considered having the following element sizes:  $h = 2, 1, 0.5, 0.25, 0.1$ , and  $0.05$   $\mu\text{m}$ . Due to the number of elements in the finest mesh ( $\approx 130,000$  elements), Fig. 3(b) only shows that various mesh refinements in one of the grains of the microstructures.

Fig. 4 illustrates the stress distribution for the six meshes. The interfacial parameters used for this simulation are  $T_{\max} = 10$  GPa and  $K_{IC} = 2$  MPa m<sup>1/2</sup>. It should be noted that the stress concentration becomes more significant for the finest mesh as expected. Microcracking did not occur in any case, even for the finest mesh, because of the high value of interfacial strength used in these simulations. The distribution of effective stress is

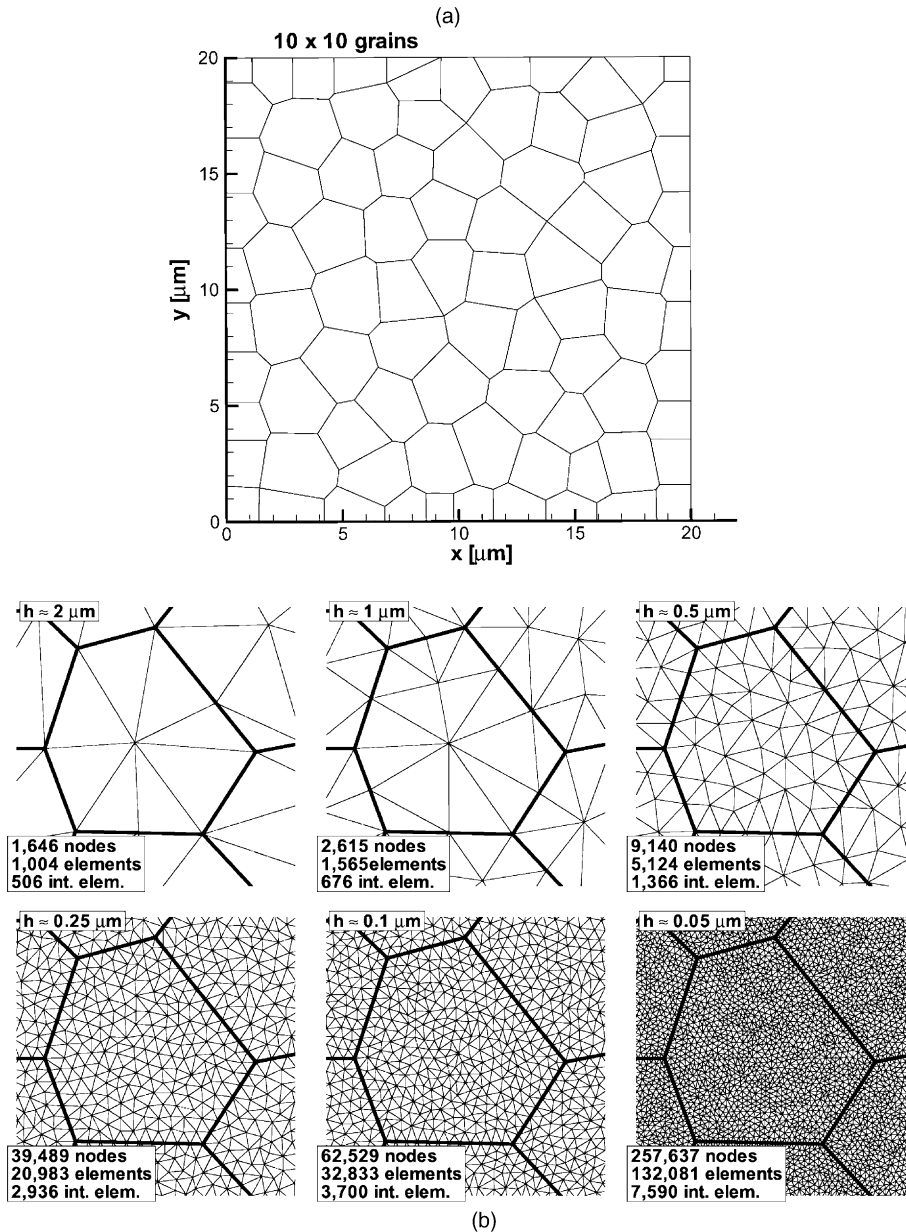


Fig. 3. (a) Geometry with  $10 \times 10$  grains to study the effect of RVE size. (b) Zoom of one of the grains showing the different mesh refinements.

similar for the meshes with  $h = 0.1$  and  $0.05 \mu\text{m}$  indicating solution convergence.

Another interesting result showing the effect of stress concentration due to a distribution of initial defects, can be seen in Fig. 5. Also in this case a

similarity in the stress distribution can be observed for the two most refined meshes. Figs. 4 and 5 are snapshots of the microstructures at 3.5 ns, right after the tensile pulse is generated in the middle of the RVE.

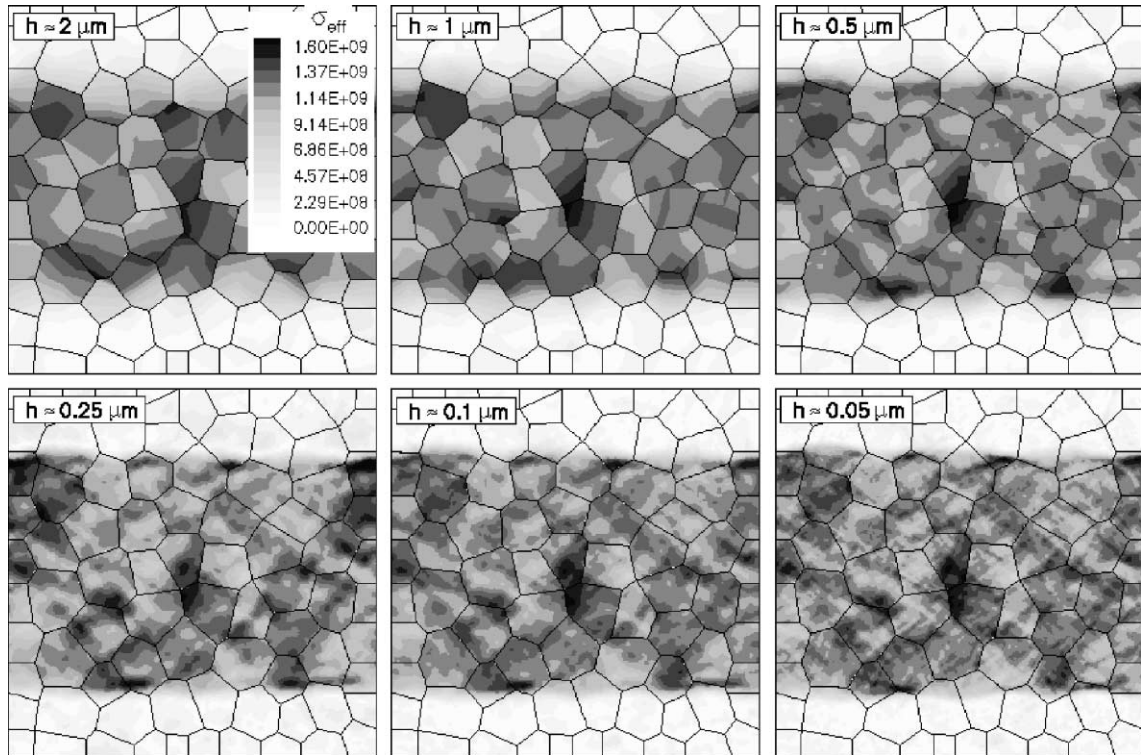


Fig. 4. Contours of effective stress for six different mesh refinements, at 3.5 ns, right after the tensile pulse develops within the RVE.

Although the above results showed that convergence of the stress distribution is achieved for element sizes of the order of  $0.1 \mu\text{m}$ , a study of convergence after microcrack initiation needs to be carried out. To address this issue, a similar simulation was performed considering a microstructure with an initial crack. The objective of this study was also to analyze the crack propagation behavior for different mesh refinements. Fig. 6 shows the distribution of the four stress component  $\sigma_{yy}$  right after the tensile pulse is generated in the middle of the RVE. As expected, the stress concentration near the crack tip becomes more important for the fine meshes. Fig. 7(a) shows the velocity at the back of the RVE (after correction due to the material impedances). The pullback signal, right after the end of the first compressive pulse, for the coarser meshes ( $h = 1$  and  $2 \mu\text{m}$ ), indicates that the crack propagates at a lower speed than in the case of the finer meshes. This is confirmed in Fig. 7(b), where the evolution of the crack length for coarser

meshes is well below the ones for finer meshes. Here again, convergence is achieved when  $h = 0.1 \mu\text{m}$ .

For a case with  $T_{\text{max}} = 1 \text{ GPa}$  and  $K_{\text{IC}} = 2 \text{ MPa m}^{1/2}$ , according to Eq. (11) the maximum allowable element size is  $h \approx 10 \mu\text{m}$ . Fig. 8(a) and (b) shows the evolution of the effective stress and crack length for two mesh sizes:  $h = 1 \mu\text{m}$  and  $h = 0.1 \mu\text{m}$ , respectively. The figure illustrates the effective stress and crack pattern at various times after the tensile pulse is generated in the middle of the RVE. Even though the stress distribution is more defined in the case with  $h = 0.1 \mu\text{m}$ , the crack pattern for both meshes is exactly the same. Fig. 9 shows the evolution of the crack density for both cases (plus a simulation with  $h = 0.05 \mu\text{m}$ ), showing clearly that convergence is achieved even when  $h = 1 \mu\text{m}$  in agreement with the requirement set by Eqs. (11) and (16).

In addition to this convergence study, linear and quadratic interface elements, including two



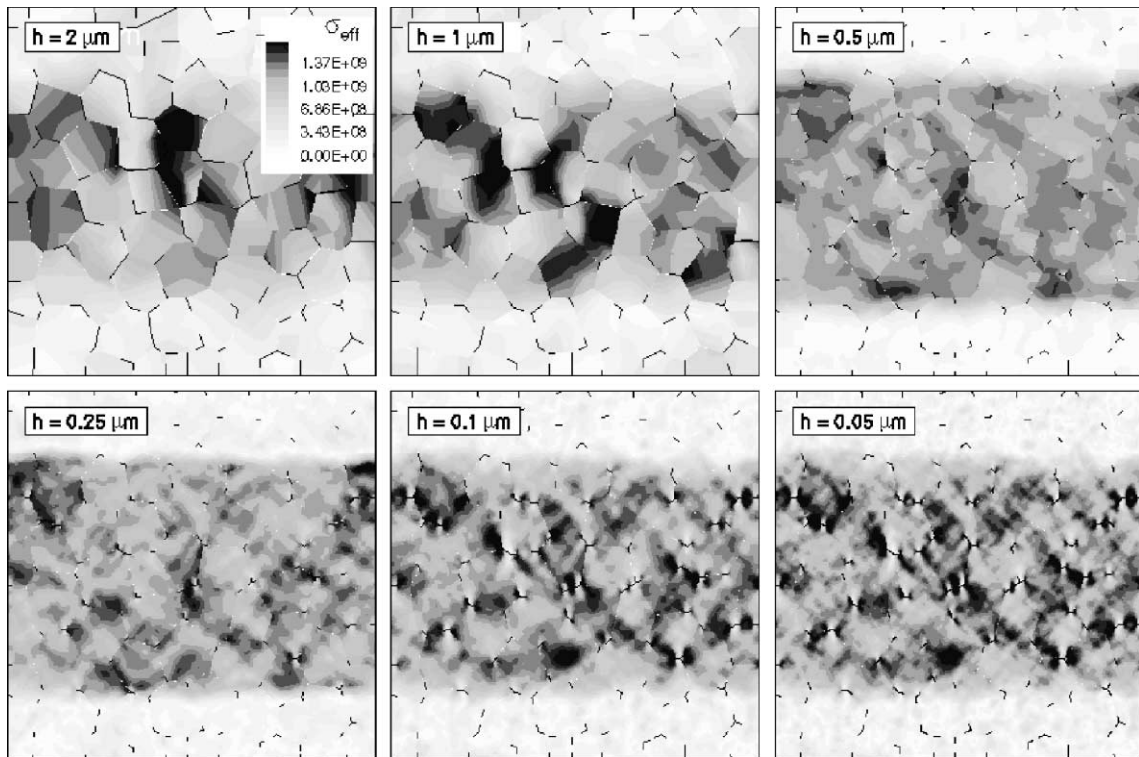


Fig. 5. Contours of effective stress for different mesh refinements. An initial distribution of flaws has been included to examine the effect of stress concentration in the finer meshes.

and three quadrature point integration schemes, have been evaluated. The results have shown no major difference between each other. Although the shape functions of the quadratic interface element are compatible with the shape functions of the six-noded triangular element, the responses of both interface elements are similar when only micro-cracking is considered as the main source of inelasticity. The difference can be only observed when geometrical and material nonlinearities are present in the simulation, such as the case where there is plasticity near the crack tip zone.

One of the most important features in the analyses is the consideration of grain anisotropy. For a case without initial defects, glassy phase, pores or any other defect in the microstructure, the only feature leading to stress concentration at triple points is grain anisotropy. To reveal the importance of this effect, simulations with and without grain anisotropy were carried out. Fig. 10 shows

the evolution of the stress distribution right after the tensile pulse is generated in the middle of the RVE for both cases. The results demonstrate that stress concentration is only present in the case with grain anisotropy, while the stress distribution is completely uniform for the isotropic case. Likewise, the presence of interface elements does not affect the uniform stress distribution observed in the isotropic case.

## 5. A parametric study

The focus of this section will be the investigation of various geometrical and physical parameters that characterize ceramic microstructures and their effect on the material response under dynamic loading. Special attention is placed on requirements leading to proper finite element simulations in the context of the proposed model. Microstructures

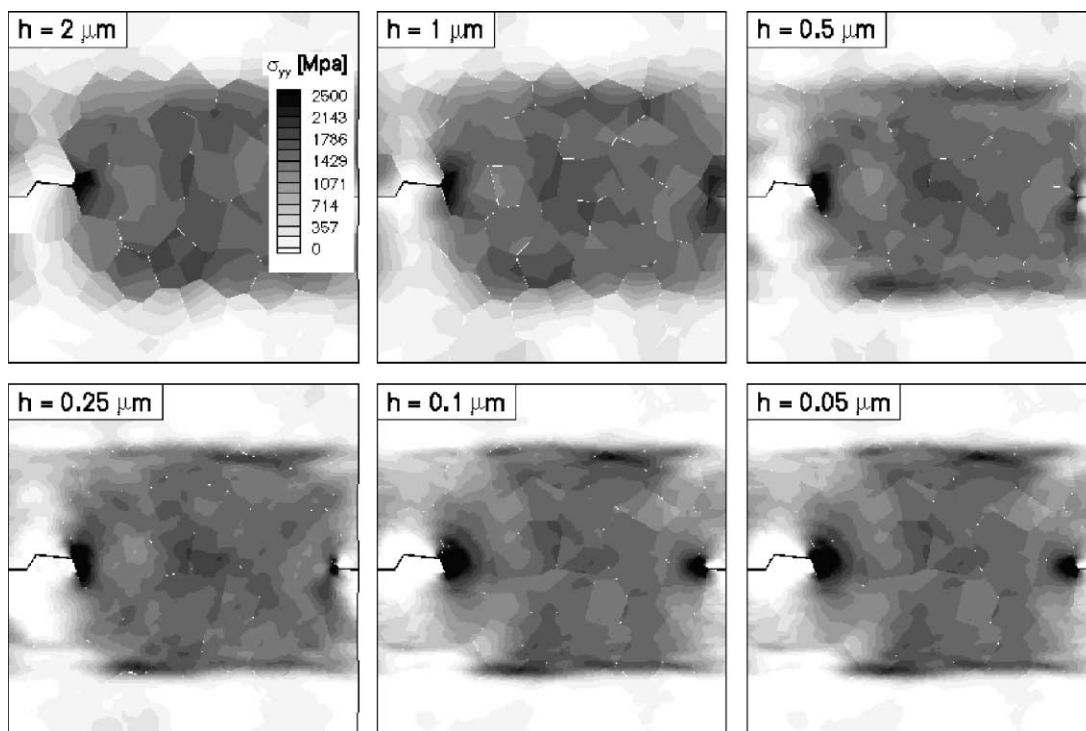


Fig. 6. Distribution of the stress component  $\sigma_{yy}$  for a microstructure with an initial crack. The convergence is clear for the finer meshes ( $h = 0.1$  and  $0.05 \mu\text{m}$ ).

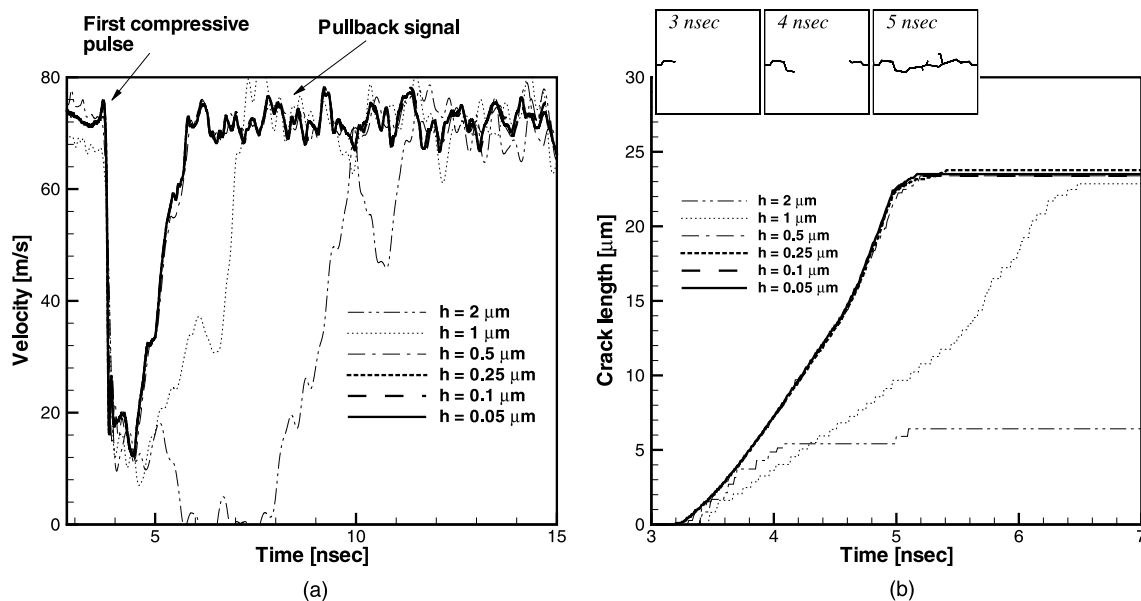


Fig. 7. (a) Velocity histories at the back of the momentum trap for different mesh sizes. (b) Evolution of accumulated crack length for different mesh sizes. Crack pattern evolution for the finest mesh, at different times, is also shown.

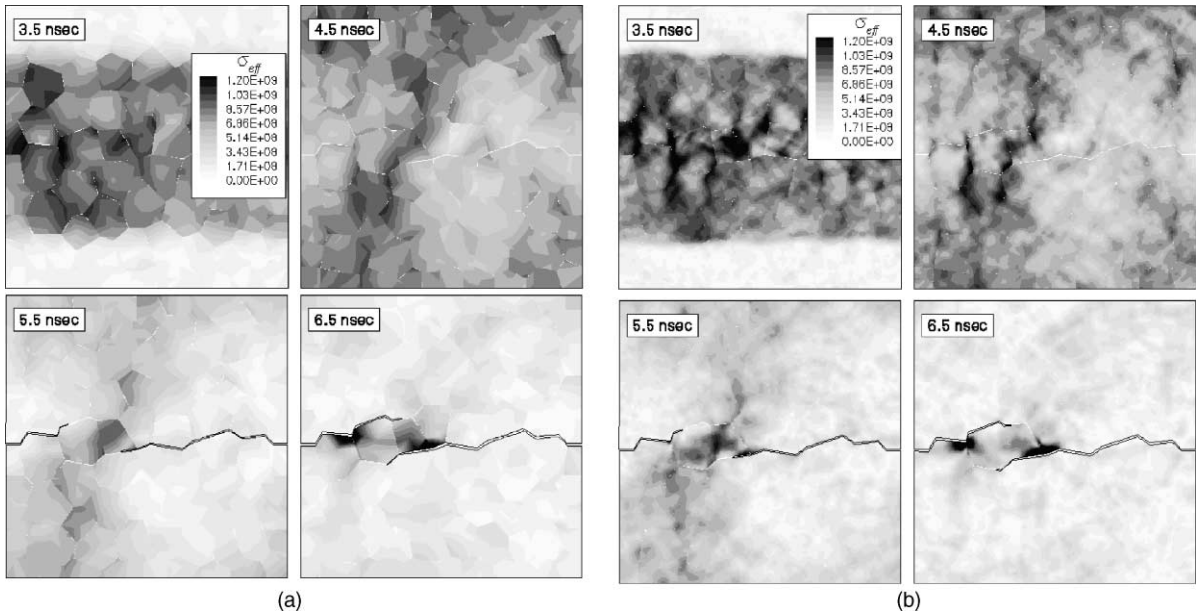


Fig. 8. Evolution of the effective stress and crack pattern for  $T_{\max} = 1$  GPa in which the required element size is  $h \approx 10 \mu\text{m}$ . (a) Coarse mesh  $h = 1 \mu\text{m}$  (b) Fine mesh  $h = 0.1 \mu\text{m}$ .

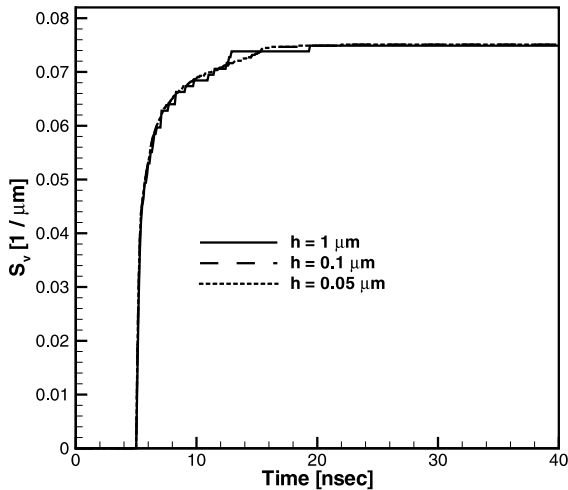


Fig. 9. Evolution of crack density for the case with  $T_{\max} = 1$  GPa and three different meshes.

with an interfacial strength of  $T_{\max} \approx 1$  GPa are considered. Since the element size required for these interfacial strength is in the range of 1–10  $\mu\text{m}$ , meshes with many grains are employed. The initial velocity used for this parametric study is

$V_0 = 86$  m/s and the duration of the tensile pulse was taken as  $\delta t = 40$  ns.

### 5.1. Effect of RVE size

Simulations were performed using three different RVEs to study the effect of the width of the computational cell. In all cases the spall region (RVE high),  $L_{\text{RVE}}$ ,  $\Delta t$  and grain size were kept the same while the width of the RVE was varied; namely 50, 100 and 200  $\mu\text{m}$ , respectively. Five sets of interface parameters were examined, viz.,  $K_{\text{IC}} = 1.7, 4, 6 \text{ MPa m}^{1/2}$  and  $T_{\max} = 0.8, 1, 1.2$  GPa.

The velocity history at the bottom of the ceramic plate is plotted in Fig. 11. The figure shows a comparison between the three RVE sizes for two different ceramics:  $K_{\text{IC}} = 4 \text{ MPa m}^{1/2}$  and  $T_{\max} = 1$  GPa, and  $K_{\text{IC}} = 6 \text{ MPa m}^{1/2}$  and  $T_{\max} = 1$  GPa. In both cases there is a pronounced pullback signal, although the slope of the signals is different. Clearly the RVE width effect is minimum. It can be observed that the major difference in the pullback signals occurs due to the differences in  $K_{\text{IC}}$ . Minor differences are associated to the RVE widths.

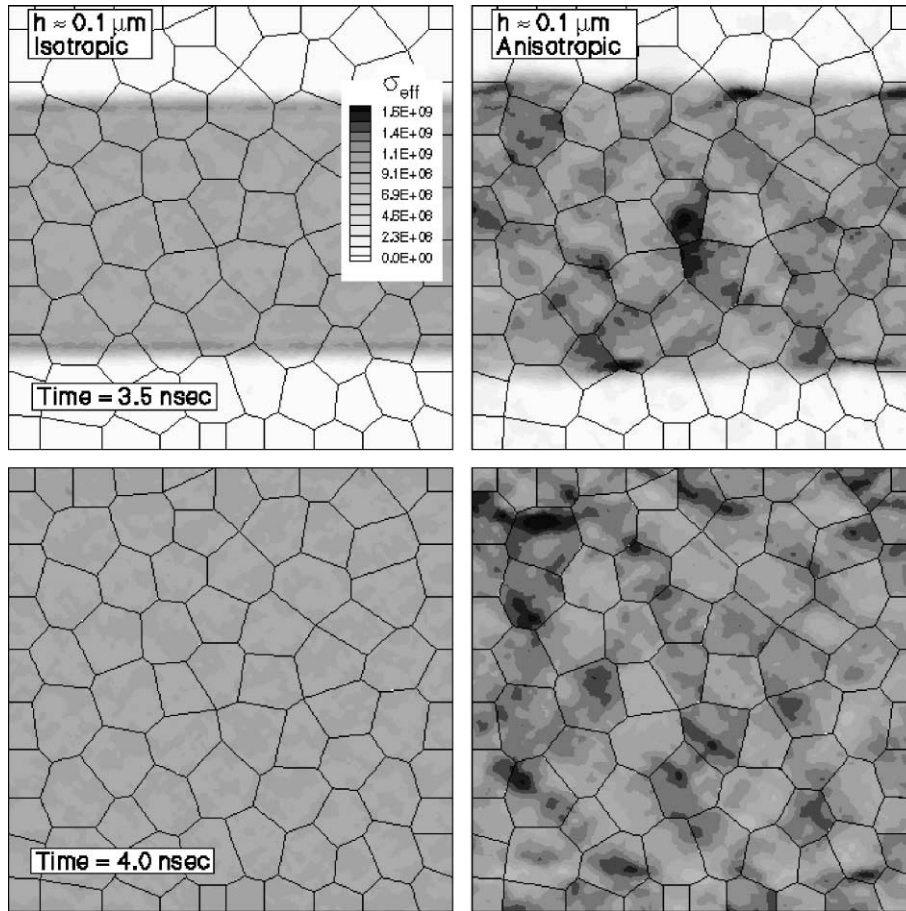


Fig. 10. Contours of effective stress at 3.5 and 4 ns for  $h = 0.1 \mu\text{m}$  with and without grain elastic anisotropy.

Fig. 12 shows the crack pattern evolution for the three RVEs with  $K_{IC} = 6 \text{ MPa m}^{1/2}$  and  $T_{\max} = 1 \text{ GPa}$ . For the narrowest case, two cracks initiate at the RVE boundaries at about 161 ns and then a third crack initiates in the middle of the RVE at 162 ns. The cracks propagate until they coalesce forming a major crack. A few grains are surrounded by the microcracks during the growth phase. For the second and third RVEs (width = 100 and 200  $\mu\text{m}$ ) something similar occurs except that in these cases the first two cracks do not initiate on the boundaries. At about 162 ns more cracks nucleate. Coalescence into a major crack occurs at about 185  $\mu\text{s}$  in all cases.

It can be concluded that the RVE width is directly related to the periodicity of the problem, which is strongly linked to the nucleation sites.

Considering that the microcrack initiation sites will depend on the distribution of grain orientations, initial defects, stochasticity of grain boundary strength and toughness, and stress wave amplitude, the size of the computational cell is basically determined by the distance between nucleation sites. In the three RVEs being analyzed, the distance between nucleation sites slightly increases as the width of the RVE increases. Therefore, the analyst can identify the RVE size, as a function of material properties and stress wave amplitude, by performing this type of simulations.

### 5.2. Effect of $K_{IC}$ and $T_{\max}$

In this section the effect of  $K_{IC}$  and  $T_{\max}$  will be studied separately. An RVE size of 100  $\mu\text{m}$  has

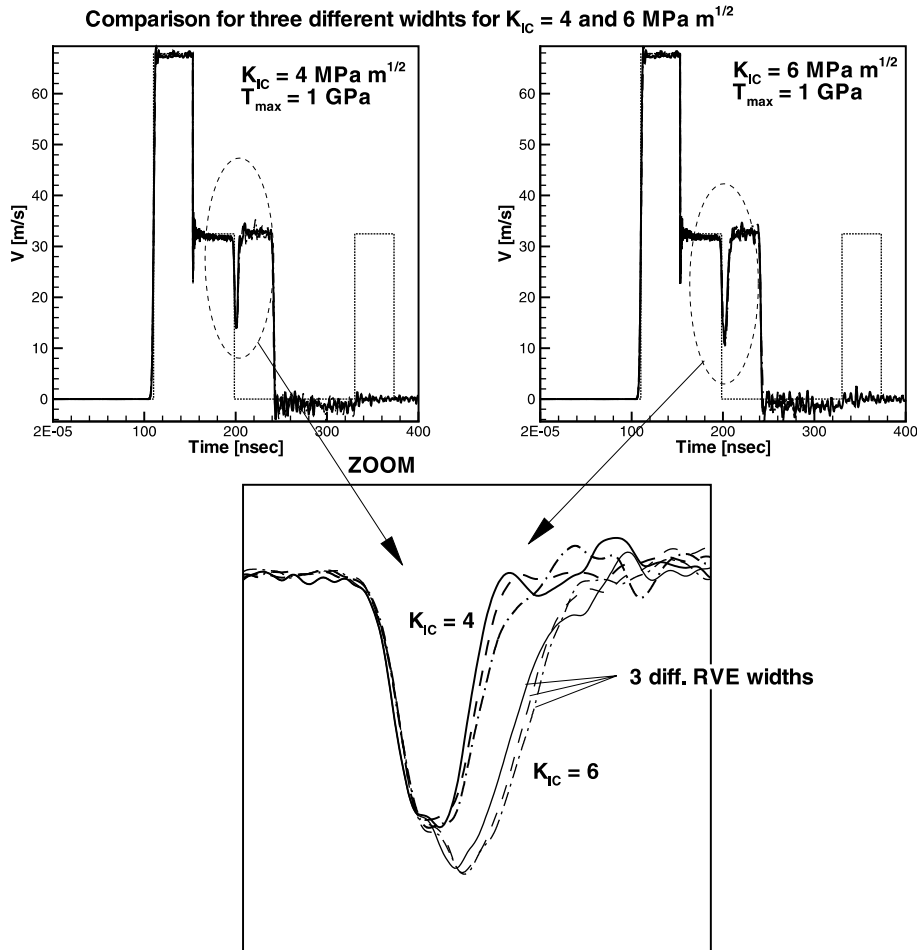


Fig. 11. Effect of RVE width: three different meshes were used for this study, with two different  $K_{IC}$ . The simulations demonstrate that the RVE size does not play an important role in the velocity history.

been utilized for these simulations in order to obtain a reasonable computational time.

#### 5.2.1. Effect of $K_{IC}$

Initial numerical simulations with  $K_{IC} = 1.7$ , 4 and  $6 \text{ MPa m}^{1/2}$  and  $T_{max} = 1 \text{ GPa}$ , were performed. After examination of results and noticing that the pullback signal was diminished as  $K_{IC}$  was increased, new simulations with higher values of  $K_{IC}$  were performed up to  $25 \text{ MPa m}^{1/2}$ . Fig. 13(a) shows the velocity at the back of the specimen for these simulations with different values of  $K_{IC}$ . For small values of  $K_{IC}$  the pullback signal is important. For  $K_{IC} = 1.7$  the duration of the pullback

signal is close to the duration of the pulse. As  $K_{IC}$  is increased, this duration decreases until  $K_{IC}$  reaches  $10 \text{ MPa m}^{1/2}$ . For this value of  $K_{IC}$ , not only the pullback signal duration decreases but also the shape and maximum pullback pulse amplitude change. For the cases with  $K_{IC} \leq 10$ , there is no second compressive pulse. Fig. 13(b) shows the entire velocity history for  $K_{IC} \geq 10 \text{ MPa m}^{1/2}$ . The shape of the second compressive pulse for  $K_{IC} = 15$  is quite different from the case with  $K_{IC} = 20 \text{ MPa m}^{1/2}$ , where its duration becomes larger than the theoretical second compressive pulse duration due to wave spreading. Fig. 14 shows the obtained crack patterns for the various

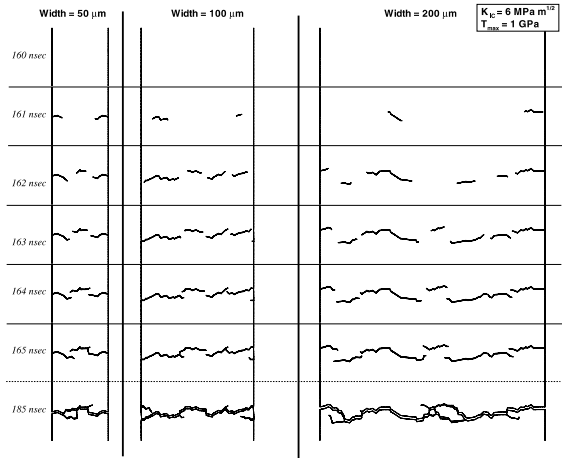


Fig. 12. Evolution of the crack patterns, during spallation, for three different RVEs with  $K_{IC} = 6 \text{ MPa m}^{1/2}$  and  $T_{max} = 1 \text{ GPa}$ . The evolution is rather similar in all three cases.

values of  $K_{IC}$ . When  $K_{IC} \geq 20 \text{ m}^{1/2}$ , there is no evidence of microcracks.

### 5.2.2. Effect of $T_{max}$

In this subsection we examine the effect of interface strength,  $T_{max}$ . Fig. 15 shows the velocity history at the back of the specimen for  $T_{max} = 0.8, 1, 1.2, 1.5, 1.6, 1.7, 1.8, 1.9, 2.0 \text{ GPa}$  when  $K_{IC}$  is

maintained at  $4 \text{ MPa m}^{1/2}$ . In this figure, only the end of the first compressive pulse and the pullback signal is displayed. It is clear from this figure that the effect of  $T_{max}$  is not as rich as the effect of  $K_{IC}$  discussed in the previous subsection.  $T_{max}$  only governs the depth of the valley, i.e., maximum stress unloading, and has almost no effect on the shape and duration of the pullback signal. It should be noted that the macroscopic stress amplitude for an initial velocity  $V_0 = 86 \text{ m/s}$  is approximately  $1.5 \text{ GPa}$ .

When the interface strength,  $T_{max}$ , reaches this value no damage is generated in the specimen, and therefore there is no pullback signal. Fig. 16 shows crack patterns for each one of the cases being examined. The crack density seems to be smaller for higher values of  $T_{max}$  until a threshold stress is reached. In all cases the width of the spall region is limited to a couple of grains.

### 5.2.3. Discussion on the effect of $K_{IC}$ and $T_{max}$

As it was demonstrated earlier, the effect of  $K_{IC}$  seems to be stronger on the shape and duration of the pullback signal than the effect of  $T_{max}$ . As  $K_{IC}$  increases, the pullback signal decreases its duration and changes its shape. As we increase  $T_{max}$  only the valley between the first compressive pulse and the

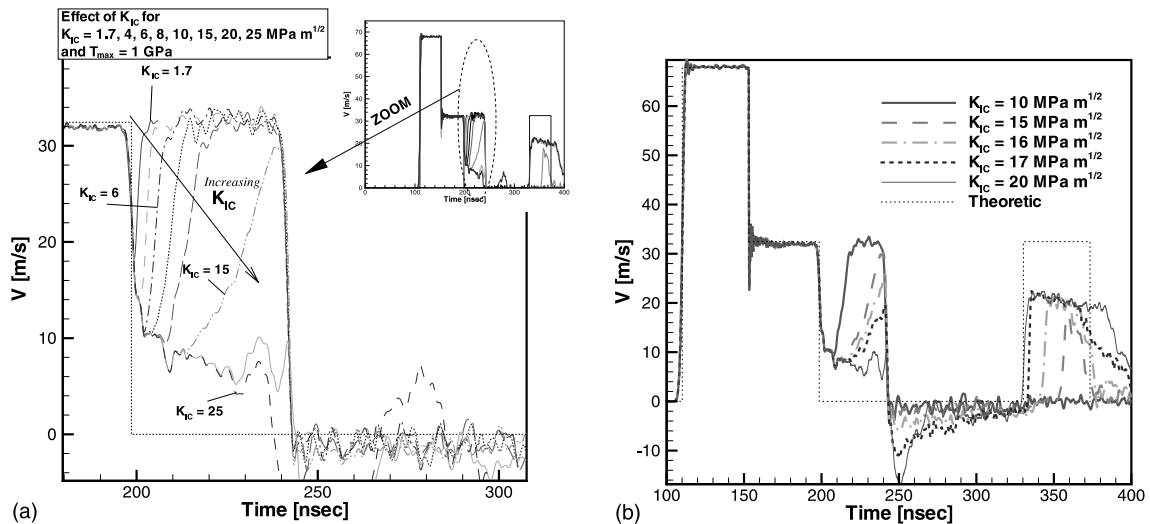
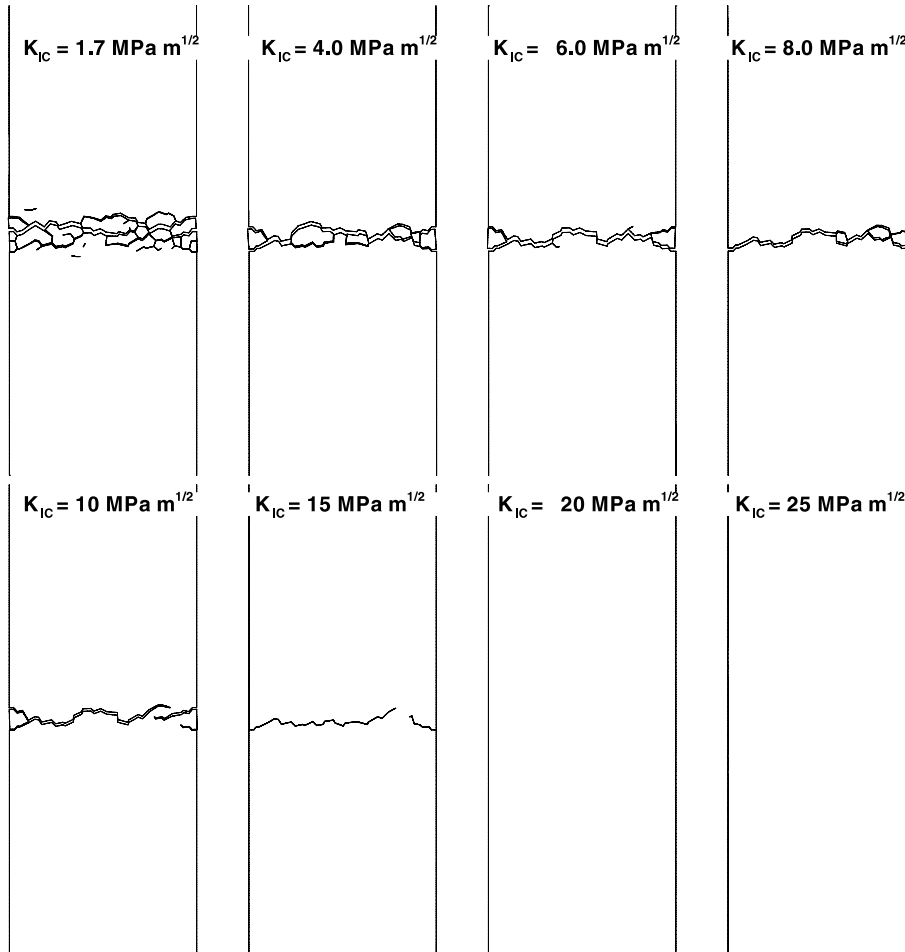


Fig. 13. (a) Effect of  $K_{IC}$  on particle velocity at the specimen-momentum trap interface. The higher  $K_{IC}$ , the smaller the pullback signal. (b) Velocity at the specimen-momentum trap interface for  $K_{IC} = 10\text{--}20 \text{ MPa m}^{1/2}$ .

Fig. 14. Effect of  $K_{IC}$  on crack pattern.

pullback signal changes. In other words, only partial unloading occurs within the material because of the generated damage. The pullback signal disappears when the grain boundary strength  $T_{max}$ , is equal or higher than the applied macroscopic stress. Fig. 17 shows the effect of these two parameters on the crack density evolution. It is noteworthy how the maximum crack density value, the crack initiation time, and the evolution rate are affected by  $K_{IC}$  while they barely change as  $T_{max}$  varies. Not only the maximum crack density value decreases as  $K_{IC}$  is increased, but also the crack initiation time is delayed. The crack initiation time is the same for different values of  $T_{max}$ .

#### 5.2.4. Synergy between $K_{IC}$ and $T_{max}$

Up to this point, the effect of  $K_{IC}$  has been studied for  $T_{max} = 1$  GPa and the effect of  $T_{max}$  for  $K_{IC} = 4$  MPa m<sup>1/2</sup>. The idea in this subsection is to present additional simulations combining the variation of both parameters at the same time in order to study the interaction and relationship between them. Fig. 18 shows six different cases or combinations of different values of  $K_{IC}$  and  $T_{max}$ ; namely,  $K_{IC} = 4, 6$  and  $8$  MPa m<sup>1/2</sup> and  $T_{max} = 1, 1.2$  and  $1.5$  GPa. These simulations clearly show that the threshold maximum strength,  $T_{max}^{th}$ , needed for eliminating damage, is dependent on  $K_{IC}$ .

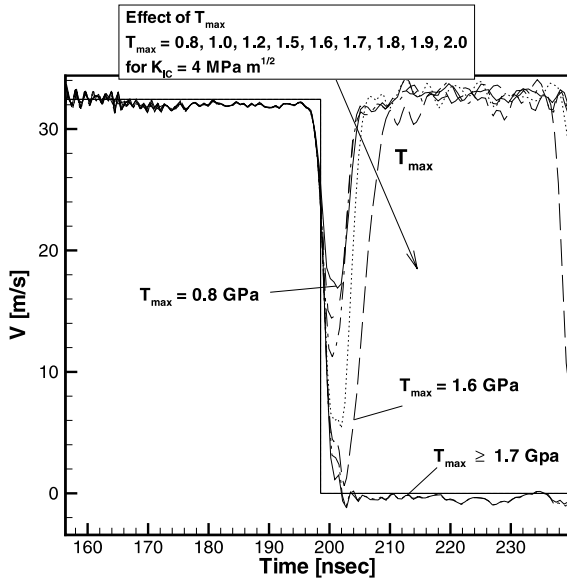


Fig. 15. Effect of  $T_{\max}$  on particle velocity at the specimen-momentum trap interface. In all cases  $K_{IC} = 4 \text{ MPa m}^{1/2}$ .

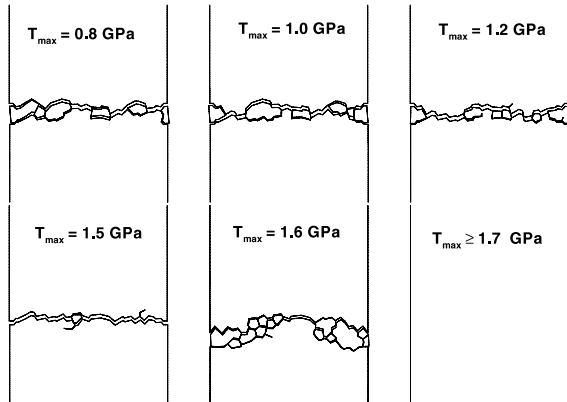


Fig. 16. Effect of  $T_{\max}$  on the crack pattern after spallation.

### 5.3. Effect of initial defects

Here the presence of initial microcracks within the RVE is examined in the context of their effect on specimen bottom surface velocity. Distributions of initial defects have been considered with 1% and 5% of interface elements broken. An RVE size of  $100 \mu\text{m}$  is utilized in the simulations. The interface element parameters used in the simulations were  $T_{\max} = 2 \text{ GPa}$  and  $K_{IC} = 4 \text{ MPa m}^{1/2}$ .

Fig. 19 shows the effect of initial defects within the RVE. As it was seen in the previous section, when  $T_{\max} = 2 \text{ GPa}$ ,  $K_{IC} = 4 \text{ MPa m}^{1/2}$  and the RVE does not contain initial defects, microcracking does not occur. Fig. 19 shows that the presence of initial defects undoubtedly affects the behavior of the specimen. Damage is not only initiated but its spreading in the spall region noteworthy. Similarly, crack bifurcation is also observed. In the 5% case, the distance between microcracks, i.e., spall region width, is reduced. A double pullback signal is predicted in the 1% case. This feature is quite interesting and illustrates how significant variations in crack kinetics can occur.

### 5.4. Stochastic effects as represented by Weibull distributions

In this subsection, the Weibull distribution of  $T_{\max}$  given by Eqs. (53) and (54) in part I has been considered for  $T_{\max}^0 = 1, 2$  and  $5 \text{ GPa}$  and  $m = 3$  and  $10$ . As it is known,  $m = 3$  approximates a Gaussian distribution, while a value of  $m = 10$  is typical of some brittle materials. An RVE size of  $100 \mu\text{m}$  and  $K_{IC} = 4 \text{ MPa m}^{1/2}$  were utilized in the simulations. Fig. 20(a) shows the two distributions,  $m = 3$  and  $10$ , for  $T_{\max}^0 = 1$  together with the crack pattern after spallation and the velocity histories at the back of the specimen. Even though it is not shown in this figure, the velocity history for the same case without a Weibull distribution, i.e., uniform strength in the RVE of  $T_{\max} = 1 \text{ GPa}$ , is almost identical to the one with  $m = 10$ .

A numerical simulation of Weibull distributions within the RVE was created, with the help of a random number generator. The minimum and maximum values of  $T_{\max}$  in the interfaces were recorded to compare the various ranges of  $T_{\max}$  and to check if the values were consistent with the assumed distributions. For the case of  $m = 3$  the minimum and maximum values of  $T_{\max}$  are  $0.19$  and  $1.6 \text{ GPa}$ , while for the case of  $m = 10$  the minimum and maximum are  $0.46$  and  $1.16 \text{ GPa}$ . In both cases, major cracks develop from side to side of the RVE and the pullback signal is significant. No major difference between  $m = 3$  and  $10$  is observed other than the level of unloading, which is higher for  $m = 10$  as expected.



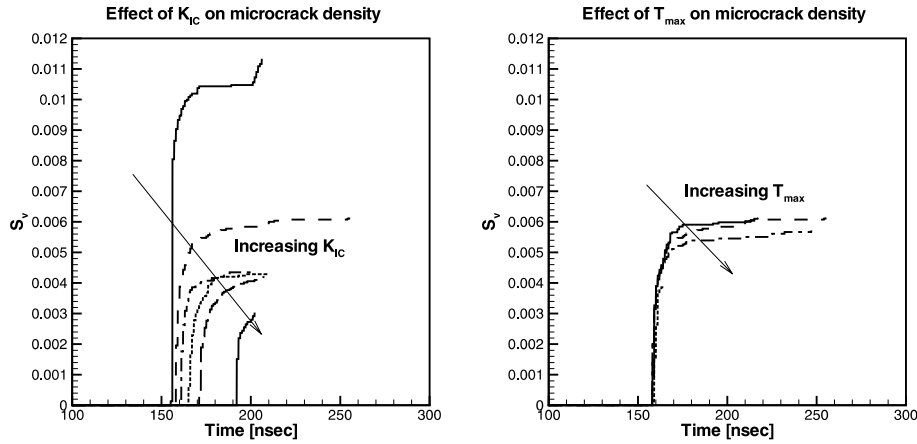
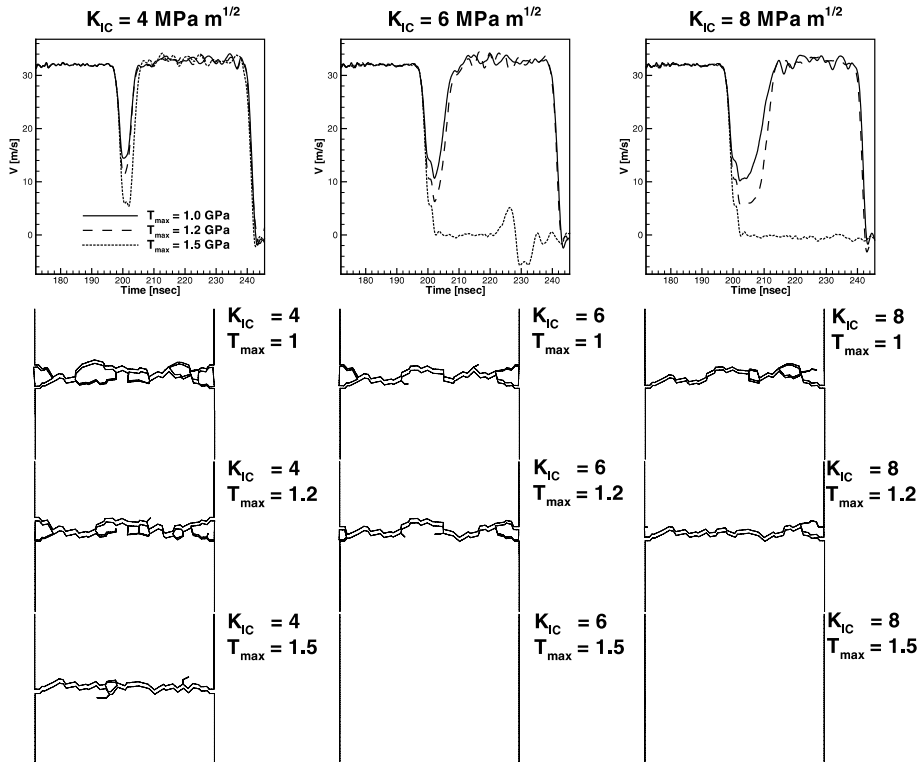
Fig. 17. Effect of  $K_{IC}$  and  $T_{max}$  on crack density evolution.Fig. 18. Plots illustrating the synergy between  $K_{IC}$  and  $T_{max}$ .

Fig. 20(b) shows the two distributions for  $T_{max}^0 = 2$  GPa. It is important to examine the plot on the upper right hand corner showing the different Weibull distributions for a given  $T_{max}^0$  so that

one can appreciate the range of  $T_{max}$  that is being considered in each analysis. For the case of  $m = 3$ , the minimum and maximum values of  $T_{max}$  are 0.38 and 3.25 GPa, while for the case of  $m = 10$  the

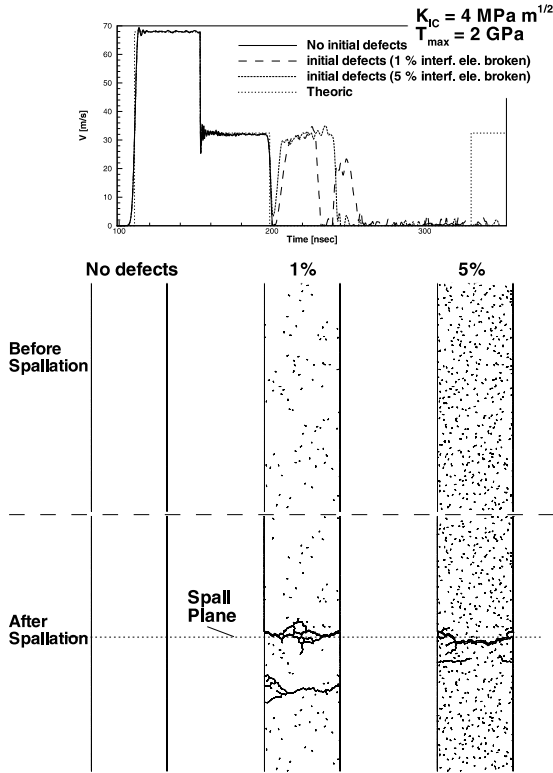


Fig. 19. Effect of initial defects, for  $K_{IC} = 4 \text{ MPa m}^{1/2}$  and  $T_{\max} = 2 \text{ GPa}$ , on particle velocity and microcracking. Zero, one and five percent of broken interface elements were considered.

minimum and maximum are 0.93 and 2.33 GPa. This analysis shows a marked difference in the velocity history and crack pattern for  $m = 3$  and 10. For the case with  $m = 10$  there is a second compressive pulse, and the formed crack is below the expected location for the spall plane. For the case with  $m = 3$  no second compressive pulse is observed and the crack propagates from side to side of the RVE in a much shorter time than the tensile pulse duration.

Fig. 20(c) shows the distribution used with  $T_{\max}^0 = 5 \text{ GPa}$ . For this case only  $m = 3$  has been plotted because when  $m = 10$  no damage is observed. The minimum and maximum values of  $T_{\max}$  are 0.85 and 9.06 GPa, respectively. The result is similar to the one for  $m = 3$ ,  $T_{\max}^0 = 2 \text{ GPa}$  consistent with the observation that if many interfaces in the RVE have a  $T_{\max}$  below the macroscopically

applied tensile stress, spallation occurs rather suddenly and the second compressive pulse disappears.

### 5.5. Rate dependent microcracking

A rate dependent cohesive surface model is proposed to examine rate effects during the creation of the fracture surfaces. In this rate dependent cohesive surface model, the cohesive strength  $T_{\max}$  is taken to be dependent on the instantaneous rate of the effective displacement jump,  $\dot{\lambda}$ . The function  $T_{\max} = f(\dot{\lambda})$  used in this analysis is given by

$$T_{\max} = T_{\max}^0 \left( 1 + \beta_2 \log \left[ \frac{\dot{\lambda}}{\dot{\lambda}_{\text{ref}}} \right] \right) \quad (17)$$

This *rate dependent model* was proposed by Espinosa et al. (1998). Another model based on an exponential law was introduced by Lee and Prakash (1999) in the study of metals. It should be mentioned that the exponential law can present problems of instabilities due to the sudden growth of  $T_{\max}$  inherent in the exponential type function. Hence, care must be exercised in its implementation. In fact, high values of  $T_{\max}$  lead to high initial slopes ( $s = T_{\max}/(\lambda_{\text{cr}}\delta)$ ) requiring smaller elements.

For this study, different values of  $\beta_2$  have been considered. The reference effective displacement jump rate is chosen as  $\dot{\lambda}_{\text{ref}} = 1 \times 10^8/\text{s}$ . The case with  $T_{\max} = 1 \text{ GPa}$  and  $K_{IC} = 4 \text{ MPa m}^{1/2}$  is examined. Fig. 21(a) shows the velocity history at the back of the specimen for  $\beta_2 = 2, 8, 10, 15, 20$  and 25. The pullback signal is clearly affected by the value of  $\beta_2$  and it tends to disappear as  $\beta_2$  is increased. Fig. 21(b) shows the crack density evolution for each one of these cases. Contrary to what one would expect, the maximum value of the crack density increases with the value of  $\beta_2$ . Fig. 22 shows even a more interesting view of this phenomenon. The crack pattern spreads and covers more area of the spall region as  $\beta_2$  is increased. As the spall region diffuses, the crack pattern is represented by a uniform distribution of individual microcracks instead of one major crack as in the cases with lower values of  $\beta_2$ .

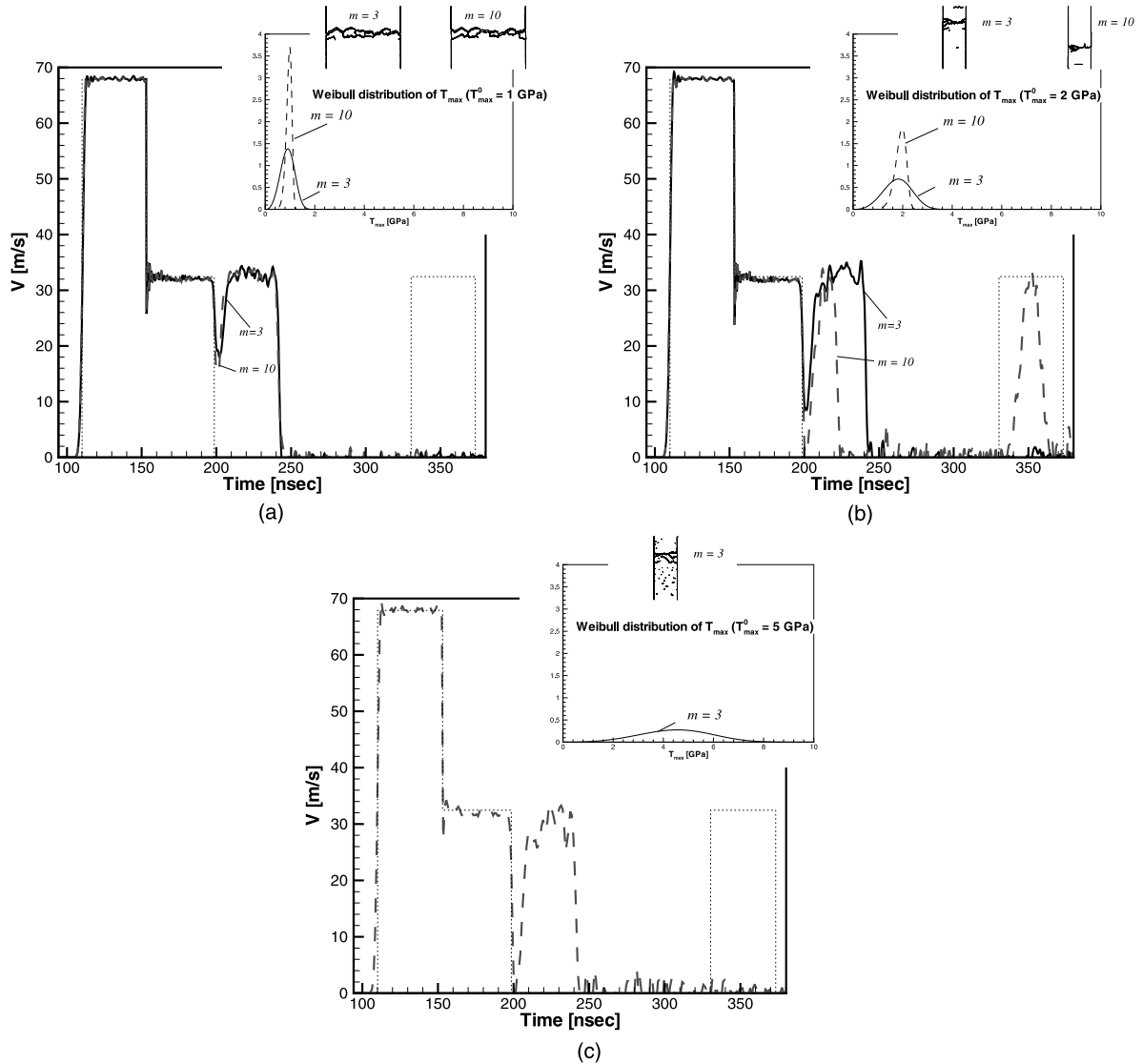


Fig. 20. (a) Weibull distribution  $f(T_{\max})$  for  $T_{\max}^0 = 1$  GPa. On the upper right hand corner, both Weibull distributions ( $m = 3$  and  $10$ ) are illustrated. In the same figure the crack pattern and velocity history at the back of the specimen are plotted. (b) Weibull distribution  $f(T_{\max})$  for  $T_{\max}^0 = 2$  GPa. On the upper right hand corner, both Weibull distributions ( $m = 3$  and  $10$ ) are illustrated. The crack pattern and velocity history at the back of the specimen are plotted. (c) Weibull distribution  $f(T_{\max})$  for  $T_{\max}^0 = 5$  GPa. On the upper right hand corner, both Weibull distributions ( $m = 3$  and  $10$ ) are illustrated. In the same figure the crack pattern and velocity history at the back of the specimen are plotted.

A similar study has been performed for  $\beta_2 = 10, 15, 20$  and  $25$ , and  $\dot{\lambda}^{\text{ref}} = 0.5 \times 10^8$  1/s. The effect of using smaller values of  $\dot{\lambda}^{\text{ref}}$  is similar to shifting the curves of  $T_{\max}/T_{\max}^0$  to the left, which means that for lower values of  $\dot{\lambda}^{\text{ref}}$ ,  $T_{\max}$  is higher for a fixed  $\dot{\lambda}$ . Fig. 23 shows the effect of  $\dot{\lambda}^{\text{ref}}$  for

$\beta_2 = 10, 15, 20$  and  $25$ . The second compressive pulse is observed for  $\beta_2 = 20$  and  $25$ , but its shape is not consistent with experimental results. In fact, the shape of the second compressive pulse is similar to the ones obtained with very high values of  $K_{\text{IC}}$ .

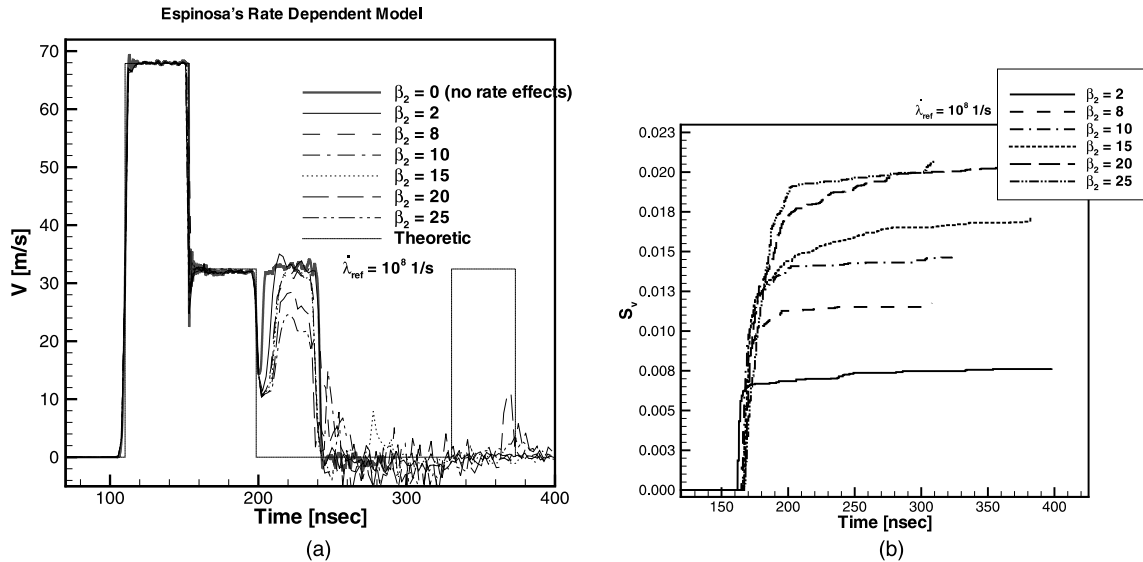


Fig. 21. (a) Espinosa's rate dependent model prediction of velocity histories for  $\beta_2 = 2, 8, 10, 15, 20$  and  $25$ , and  $\dot{\lambda}_{ref} = 1 \times 10^8$  1/s. (b) Evolution of crack density for different values of  $\beta_2$  and  $\dot{\lambda}_{ref} = 1 \times 10^8$  1/s.

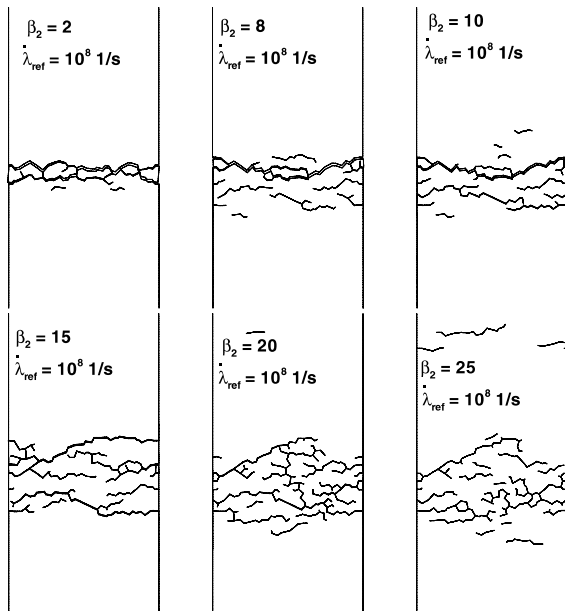


Fig. 22. Effect of  $\beta_2$  on crack pattern.

Fig. 24(a) shows this effect on the evolution of the crack density. The crack initiation time is delayed for smaller values of  $\dot{\lambda}$  while the slope remains almost identical, except that the maximum

crack density behaves differently for both  $\dot{\lambda}_{ref}$ . Contrary to what happens with  $\dot{\lambda}_{ref} = 1.0 \times 10^8$ /s, in the case with  $\dot{\lambda}_{ref} = 0.5 \times 10^8$ /s the maximum crack density decreases as  $\beta_2$  is increased. Fig. 24(b) shows the crack pattern for each  $\beta_2$  and  $\dot{\lambda} = 0.5 \times 10^8$ /s. The behavior observed in the previous case, now it is more pronounced leading to a diluted crack pattern when  $\beta_2 = 25$ . It should be noted that such crack pattern is not consistent with experimental observations (Espinosa et al., 1992).

## 6. Simulations with high values of $T_{max}$ (strong ceramics and composites)

High purity ceramics are synthesized such that their grain boundary strength can reach values of about  $E/40$  or even  $E/20$ . In this section a parametric study of the effect of cohesive law parameters is given when  $T_{max} = 10$  GPa. The initial velocity is chosen to be  $V_0 = 92$  m/s and the pulse duration  $\delta t = 25$  ns; these values correspond to one of the experiments performed by Raiser et al. (1994). The purpose of this study is to demonstrate that the effect of various model parameters are

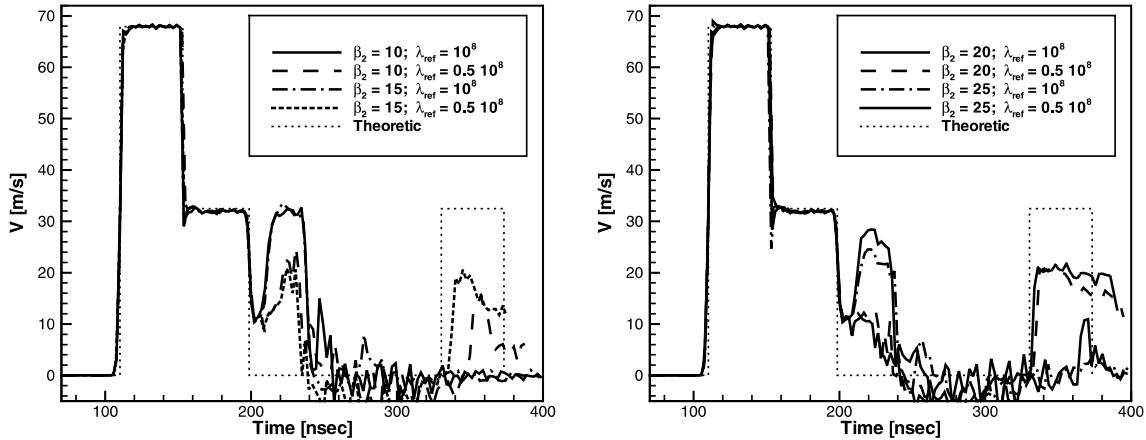


Fig. 23. Espinosa's rate dependent model prediction of velocity histories for  $\beta_2 = 10, 15, 20$  and  $25$ , and  $\dot{\lambda}^{\text{ref}} = 0.5 \times 10^8 \text{ 1/s}$ .

similar to what was presented when  $T_{\text{max}} \approx 1 \text{ GPa}$ . Unique and interesting features are observed in the case of strong ceramics.

As discussed in the convergence analysis, when high values of  $T_{\text{max}}$  are examined, e.g.,  $T_{\text{max}} = 10 \text{ GPa}$  and  $K_{\text{IC}} = 2 \text{ MPa m}^{1/2}$ , the element size required for simulations is in the range  $h = 0.1\text{--}0.2 \text{ }\mu\text{m}$ . This means that the analyst will have to carefully select the appropriate RVE to limit the computational time. The principal factors for this choice are

1. Periodicity: The periodicity of the problem, and therefore the width  $W$  of the RVE is linked to the distance between crack nucleation sites. This periodicity does not depend only on the geometry (grain shape and size, distribution of initial flaw, pores or glassy phase) but also depends on the loading conditions (impact velocity  $V_0$ , and pulse duration  $\delta t$ ).
2. Extent of microcracking: It was experimentally observed that microcracks propagate and coalesce in the so-called *spall region* (Espinosa et al., 1992); this spall region depends on the grain size and morphology. Typically, microcracks propagate in a region consisting of two or three grains above and below the spall plane. However, the height  $H$  of the RVE has to be chosen such that there are several rows of grains between the spall region and the top and bottom boundaries in order to avoid boundary effects arising

from condition of uniform displacement and velocity imposed by the viscous boundary conditions representing the homogenized ceramic.

In the following subsections a parametric study is presented with an RVE size of  $20 \times 20 \text{ }\mu\text{m}^2$  and a grain size of  $2 \text{ }\mu\text{m}$  ( $10 \times 10$  grains). The interface strength considered in all these cases is chosen to be  $T_{\text{max}} \approx E/40 = 10 \text{ GPa}$ . In some cases the width of the RVE is enlarged to study the effect of periodicity on crack nucleation, propagation and coalescence.

#### 6.1. Effect of crack initiation distance on propagation and branching

In this study, the crack propagation pattern is enriched by a stochastic distribution of grain boundary strength and toughness. The Weibull parameters used in the simulations were:  $T_{\text{max}}^0 = 10 \text{ GPa}$ ,  $K_{\text{IC}}^0 = 2 \text{ MPa m}^{1/2}$  and  $m = 10$ . An initial crack of a few microns is considered on the side of the RVE. Three RVEs are considered, the height is  $20 \text{ }\mu\text{m}$  in all the cases while the width is  $20, 40$  and  $60 \text{ }\mu\text{m}$ , respectively. The idea of considering different RVE width with only one initial crack is to study the effect of nucleation sites distance on material response.

Fig. 25 shows the crack pattern and stress ( $\sigma_{yy}$ ) evolution for the case with an RVE of  $60 \times 20$

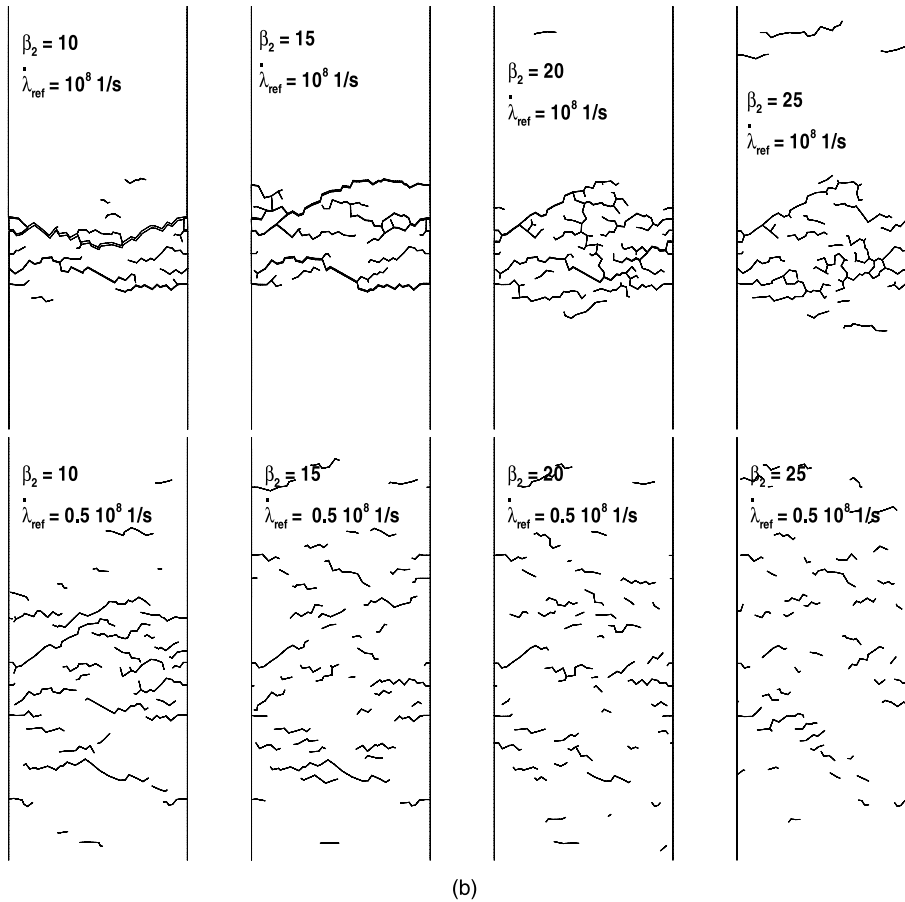
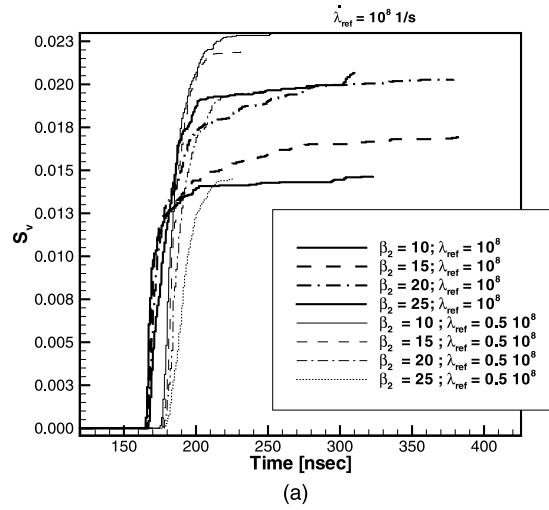


Fig. 24. (a) Evolution of the crack density using the rate dependent model and various values of  $\beta_2$  and  $\dot{\lambda}^{ref} = 0.5 \times 10^8 \text{ 1/s}$ . (b) Effect of  $\beta_2$  on the crack pattern.

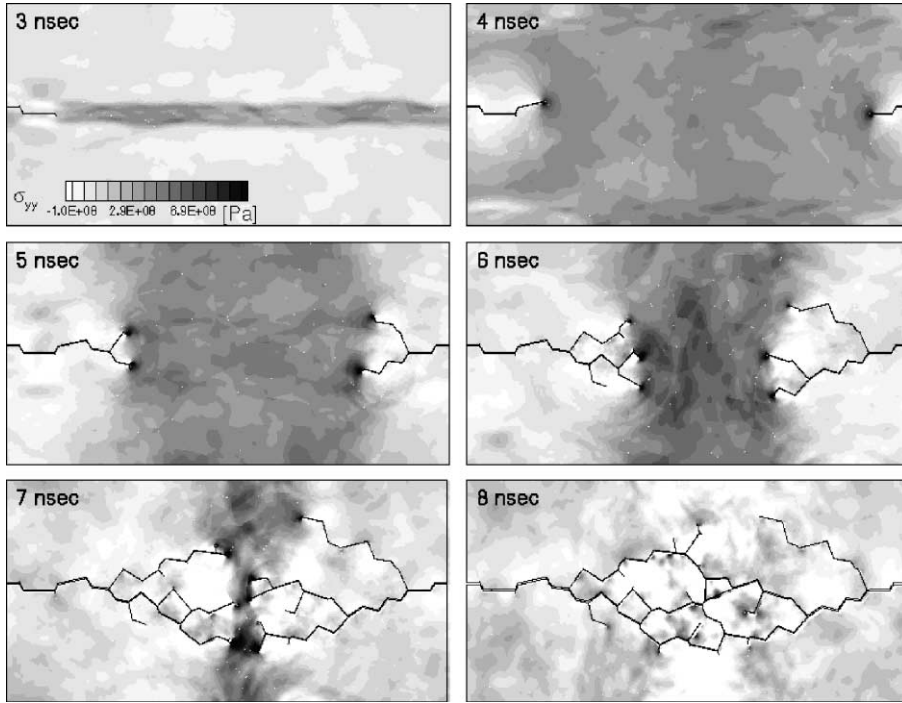


Fig. 25. Evolution of  $\sigma_{yy}$  on a  $60 \times 20 \mu\text{m}^2$  RVE containing an initial crack. The tensile pulse develops at 3 ns and it propagates through the ceramic until crack coalescence.

$\mu\text{m}^2$ . The crack starts propagating at 3 ns (when the tensile pulse reaches the spall plane) and propagates until coalescence. Crack branching is observed at 5 ns. Fig. 25 clearly shows the stress concentration at the crack tips for each branch.

The effect of distance between nucleation sites, for the different RVEs, is illustrated in Figs. 26 and 27. The  $20 \times 20 \mu\text{m}^2$  RVE corresponds to a case where there is a nucleating crack every  $20 \mu\text{m}$ , the  $40 \times 20 \mu\text{m}^2$  RVE corresponds to the case where

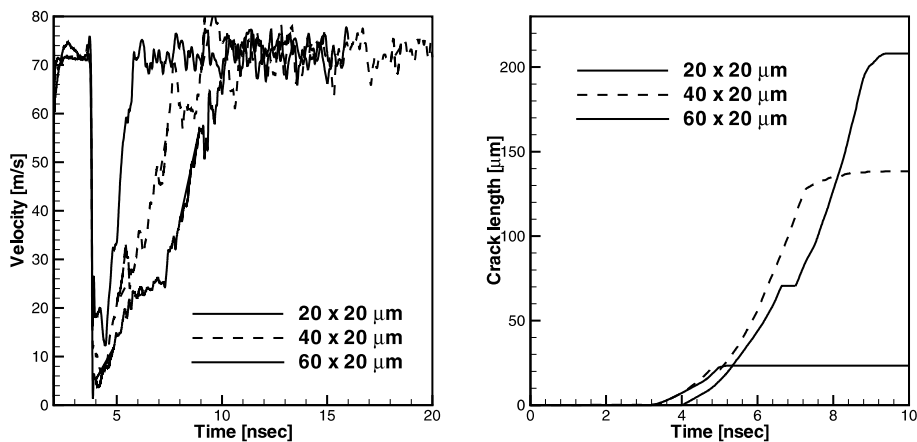


Fig. 26. Effect of distance between crack nucleation sites on velocity history and crack length evolution.

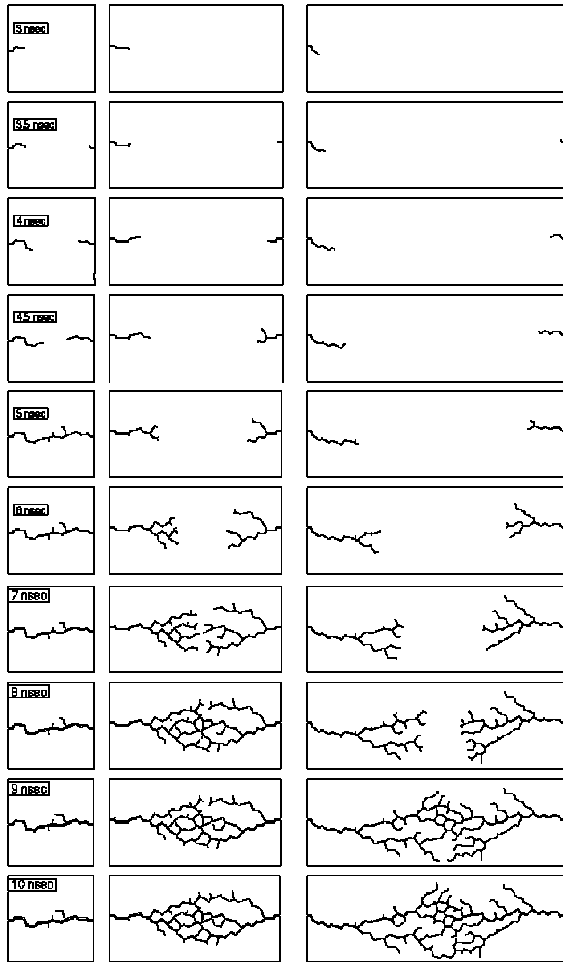


Fig. 27. Crack pattern evolution for three different RVEs.

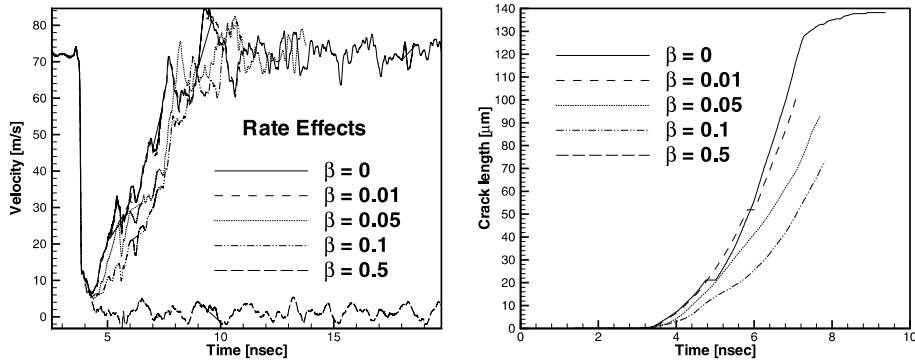
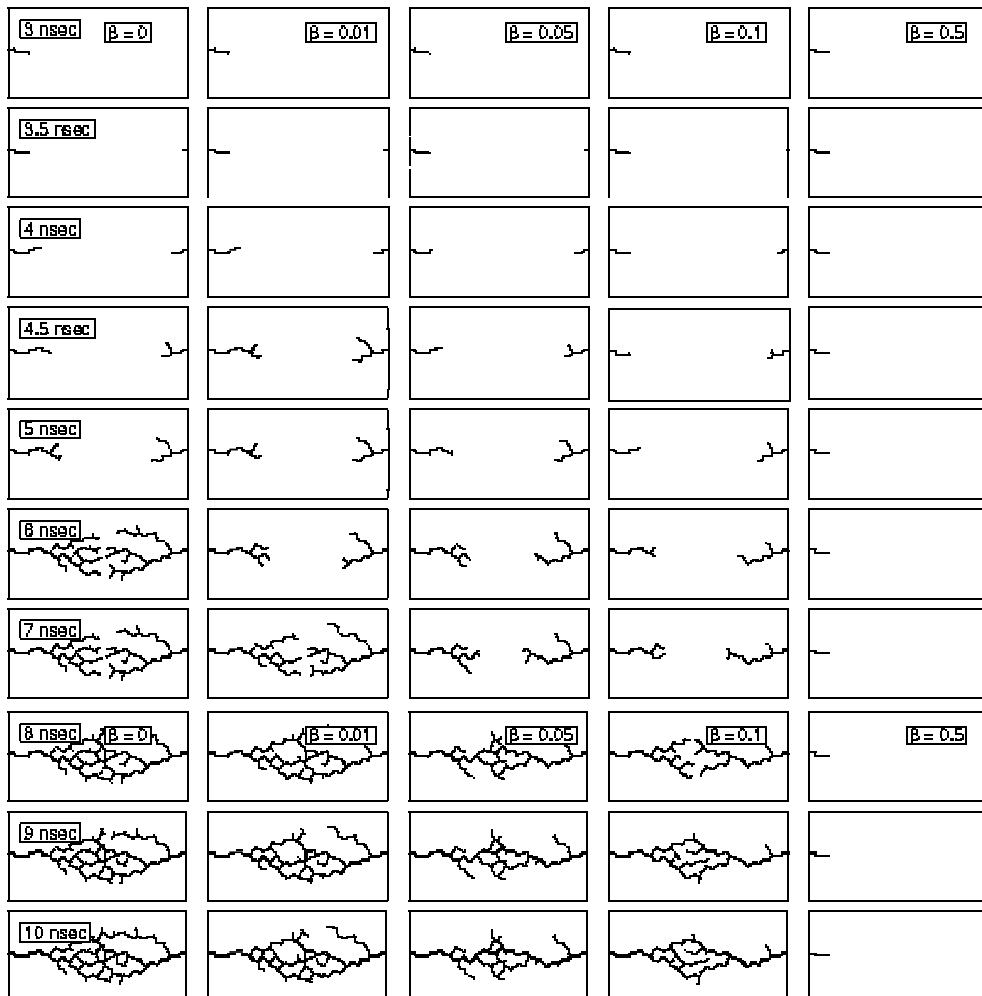
there is a nucleating crack every 40  $\mu\text{m}$ , and the  $60 \times 20 \mu\text{m}^2$  RVE to the case where there is a nucleating crack every 60  $\mu\text{m}$ . By examining the crack length history, Fig. 26 (right), one can notice that although the initial slope of the accumulated crack length is almost the same for all three cases, the pullback signal is more pronounced in the case with the highest density of nucleation sites, i.e., nucleation sites every 20  $\mu\text{m}$ . These findings illustrate the fact that the pullback signal represents a combination of two factors, the crack speed and the time the crack takes to coalesce with its neighbors.

Fig. 27 shows the crack pattern evolution for each one of the three cases. For the  $20 \times 20 \mu\text{m}^2$

RVE, crack branching is inhibited, because coalescence occurs before the onset of branching. For the  $40 \times 20$  and  $60 \times 20 \mu\text{m}^2$  RVEs, the crack branches and the degree of branching is more pronounced for the largest RVE, i.e., when the distance between nucleating sites increases.

Fig. 28 illustrates rate effects for the  $40 \times 20 \mu\text{m}^2$  RVE. Even though the accumulated crack length history seems to be significantly dependent on  $\beta_2$  (hereafter  $\beta$ ), the velocity history is not strongly affected when  $\beta \sim 0.1$ . In fact, Fig. 29 shows the evolution of the crack pattern for the various cases. An interesting observation is that rate effects delay and/or inhibit crack branching. This feature explains the observed differences in accumulated crack length evolution. The speed at which the crack propagates and coalesce, with neighbor cracks, does not seem to change with rate effects, but the capability of the ceramic to branch does. The variation on the accumulated crack length evolution is due to this factor. The crack accumulated length is reduced as  $\beta$  increases. A similar effect is observed for different values of  $K_{IC}$ . Fig. 30 shows how branching tends to disappear when  $K_{IC}$  increases. The similarity between rate effects and toughness, on the pull back signal, were previously highlighted. As one would expect, crack branching in the form of a “funnel” is not only dependent on rate effects but also on the value of  $K_{IC}$ , which is directly related to the dissipated energy at the interfaces. This means that in low toughness ceramics, branching will be more likely than in ceramics with tough interfaces where the energy needed to create new surfaces is higher. It is important to keep in mind that stochasticity of the microstructure would make these patterns vary according to the different grain geometry and orientation, interface strength distribution, presence of initial defects, etc. If a considerable number of simulations with different grain orientations and interface strength distribution is carried out, a set of parameters for which crack branching would occur can be obtained. It should be noted that this kind of behavior is also observed for cases with single cracks. Ballarini (2000), observed that for a single crack a “funnel” like zone can be defined considering the stochasticity of the microstructure.



Fig. 28. Rate effects on velocity history for the  $40 \times 20 \mu\text{m}^2$  RVE.Fig. 29. Rate effects on crack pattern evolution for the  $40 \times 20 \mu\text{m}^2$  RVE.

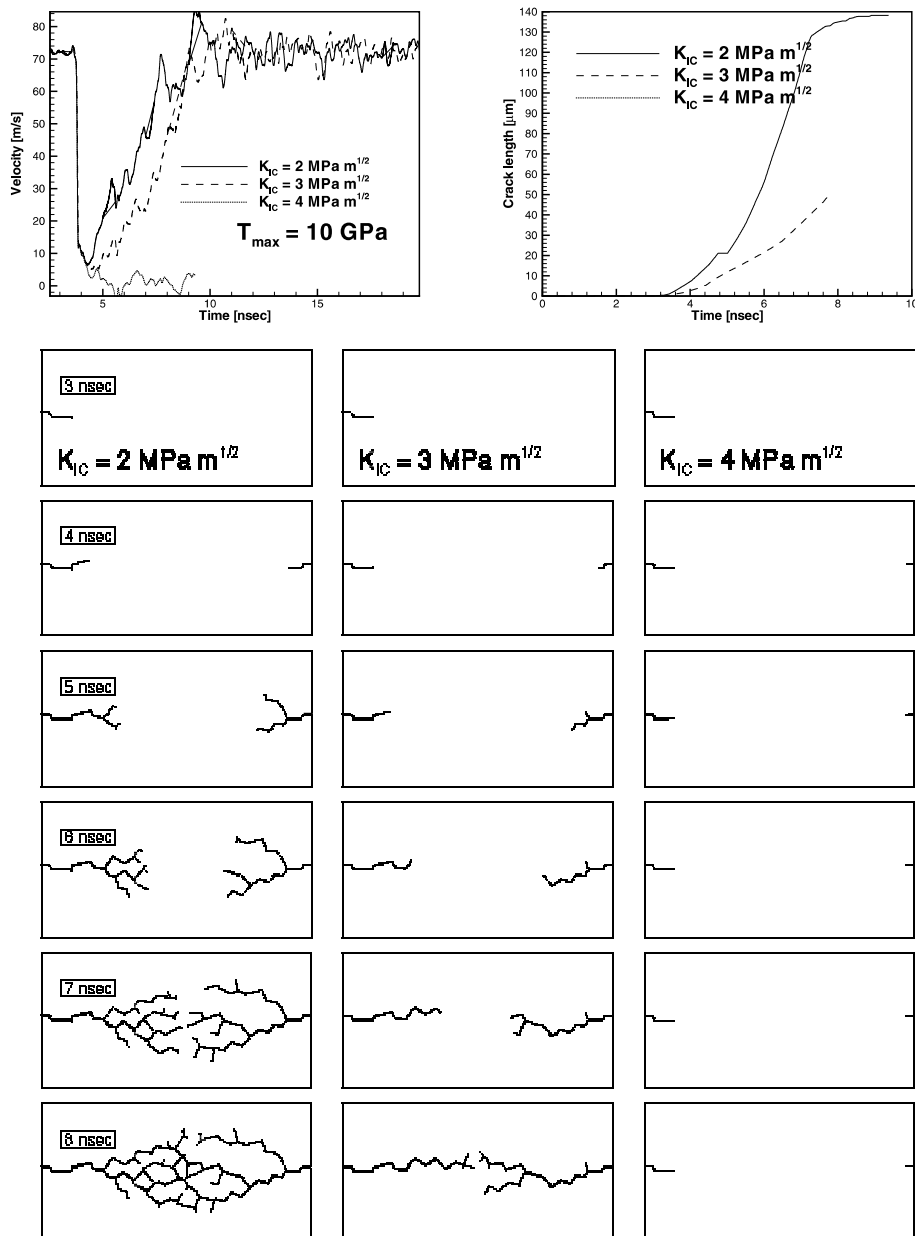


Fig. 30. Effect of  $K_{IC}$  on velocity history, crack length evolution and crack pattern.

## 6.2. Modeling residual thermal stresses and induced microcracking

Throughout the analyses discussed in previous sections, the ceramic microstructure has been ide-

alized as an ensemble of randomly oriented, elastically and thermally anisotropic grains with brittle intergranular interfaces. Nonetheless, thermal stresses and microcracking resulting from the material fabrication process were not considered.

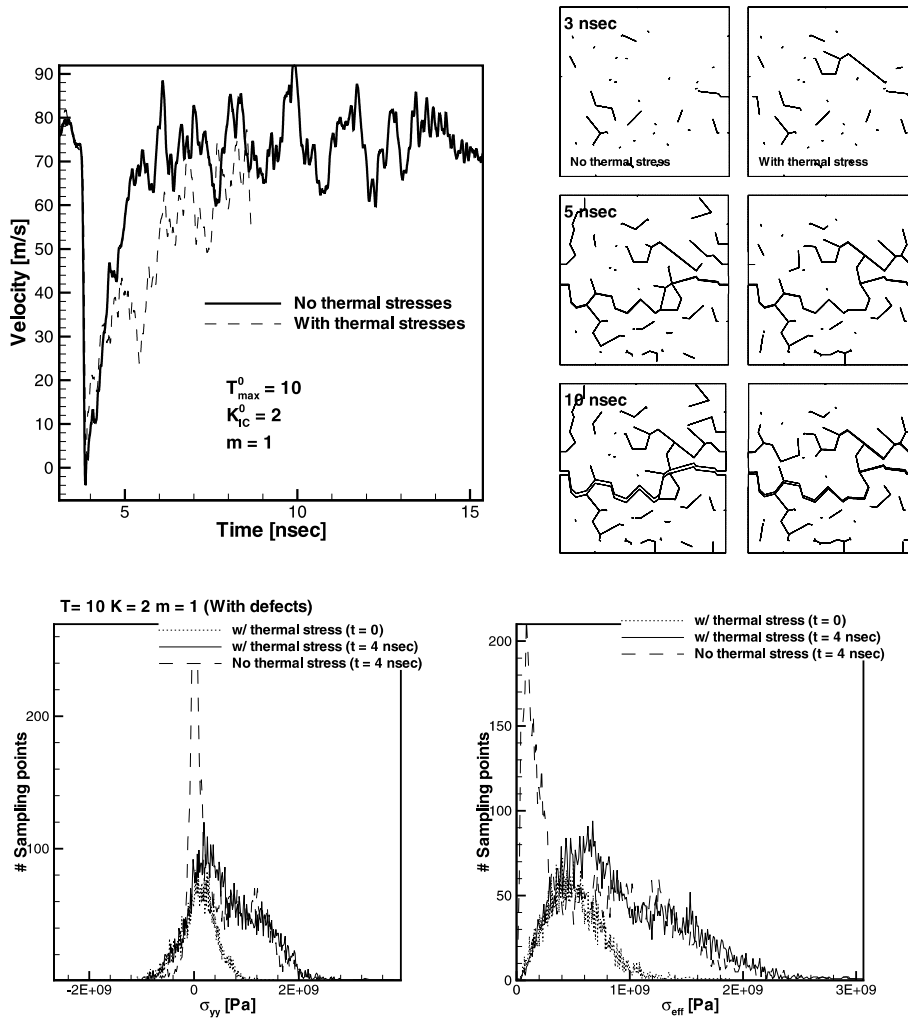


Fig. 31. Effect of thermal residual stress on velocity history, crack length evolution and crack pattern. Histograms of  $\sigma_{yy}$  and  $\sigma_{eff}$  are also included in the figure to illustrate shift due to residual stresses.

It is well known that in the sintering of ceramics, the material is brought from its fabrication temperature down to room temperature. In some ceramics, the stresses in the sample are partially relaxed, during cooling, due to creep along grain boundaries.

Since quasi-static simulations of the residual thermal stresses during cooling in the process of fabrication have been performed in the past, (Evans, 1978; Fu and Evans, 1985; Tvergaard and Hutchinson, 1988; Ortiz and Suresh, 1993; Sridhar et al., 1994), in this section we just present the ef-

fect of residual thermal stresses on the dynamic behavior of the ceramic.

Fig. 31 shows the effect of the residual stresses corresponding to a drop of 1500° K during the material fabrication process. The Weibull parameters are  $T_{\max}^0 = 10$  GPa,  $K_{IC}^0 = 2$  MPa m<sup>1/2</sup> and  $m = 1$ . Since the overall effect of the thermal residual stresses has been observed to be similar for different Weibull parameters, we have chosen these parameters for our discussion purposes. These simulations and others considering different cohesive properties, did not result in a marked tendency of

the material behavior. In some cases the ceramic seems to be stronger when the residual stresses are superimposed. Histograms of  $\sigma_{yy}$  and  $\sigma_{eff}$  for each case have been obtained to study this phenomena. It was observed that bigger RVEs need to be considered to obtain statistically significant results. In all cases the thermal stresses introduce a perturbation on the histogram of stresses when compared to the cases without thermal stresses, see Fig. 31. Such perturbation is not enough to significantly change the overall material dynamic behavior. In fact, the perturbations in stress are about 20–100 MPa, which appear to be small when compared to the applied macroscopic stress of about 1 GPa to significantly affect the onset of microcracking and its evolution. It is expected that residual thermal stresses may affect the threshold stress required for crack initiation as well as the location of initial defects in the material microstructure but do not seem to result in a significant departure from the features observed in the absence of residual stresses. These findings validate all the analyses and conclusions obtained in the absence of residual stresses.

## 7. Concluding remarks

In this paper, the micromechanical model introduced in part I was used to simulate wave propagation experiments. The numerical results are shown in terms of microcrack patterns, evolution of crack density, and velocity histories simulated at the back of the ceramic plate. Two parametric studies were performed, one for  $T_{max} \approx 1$  GPa (weak ceramics) and another for  $T_{max} \approx 10$  GPa (strong ceramics). To reduce the calculation time without changing the physics of the problem, a simplified model has been proposed and implemented. The effect of RVE size was studied along with different interface properties. Conditions under which solution convergence is obtained were derived and illustrated in Section 5.5.

Section 5.2 illustrates the effect of  $K_{IC}$  and  $T_{max}$ , in the absence of stochasticity and rate effects, on the macroscopic material response. The most important conclusion from this section is

that  $K_{IC}$  affects significantly the crack density evolution, crack pattern and pullback signal, while changes in grain boundary strength,  $T_{max}$  do not significantly affect damage evolution as long as  $T_{max}$  is below the applied macroscopic tensile stress. It is also noteworthy that the pullback signal decreases for high values of  $K_{IC}$  and that the second compressive pulse is much wider than the second compressive pulse predicted by elastic wave theory. It should be noticed that even when no cracks are observed on plotted crack patterns, damage is present in the form of energy dissipation in the interface elements (when  $T > T_{max}$  and  $\lambda < 1$ ). The way in which the energy is dissipated on the interface elements changes the shape of the second compressive pulse. Furthermore, the values of  $K_{IC}$  for which the pullback signal totally disappears are unrealistic for ceramic materials, i.e.,  $K_{IC} = 20\text{--}25 \text{ MPa m}^{1/2}$ .

Section 5.3 outlines the effect of initial defects. Different percentages of initial defects were considered. It was observed that, in some cases, the cracks do not propagate along the expected spall plane. When a spall plane is formed, distinct features such as formation of double major cracks and branching are observed. Section 5.4 shows the effect of considering a Weibull distribution on  $T_{max}$  while keeping  $K_{IC}$  constant. A study of various  $T_{max}^0$ ,  $m$  (Weibull parameter) and different fixed  $K_{IC}$  were performed. A range of responses was obtained for different sets of parameters. It was also observed that for a given set of parameters, but different *seeds*, the response changes significantly. The extreme case occurs for a distribution of  $T_{max}$  in which some interfaces exhibit  $T_{max} = 0$ .

Finally, in Section 5.5 a parametric study of rate dependent models was carried out. For the considered law, the bigger the parameter  $\beta_2$  is, the higher the  $T_{max}$  growth rate. Also, the smaller the  $\dot{\lambda}^{ref}$ , the higher the  $T_{max}$  growth rate. The most important finding was that for higher rate effects (which means for higher values of  $\beta_2$  or/and smaller values of  $\dot{\lambda}^{ref}$ ) the crack pattern presents isolated microcracks distributed on a wide region, while for smaller rate effects the microcracks concentrate very close to the crack plane approaching, asymptotically, the case without rate effects in which only one major crack forms.

In addition the following features have been identified:

1. The distribution of  $T_{\max}$  in the RVE controls maximum unloading and the onset of damage while  $K_{IC}$  strongly affects damage kinetics. The pullback signal disappears for very high values of  $K_{IC}$  but the shape of the second compressive pulse is not consistent with experimental results. All possible combinations of  $T_{\max}$  and  $K_{IC}$  have been considered and no set of parameters has been found to adequately reproduce experimental results. Therefore, other microstructural features, such as nonuniform grain size and shape distributions, need to be included to capture the velocity histories and crack patterns observed in experiments (Zavattieri and Espinosa, 2001).
2. The effect of introducing a Weibull statistics is only important for some values of  $T_{\max}$ . If the value of  $T_{\max}^0$  is not close to a representative value for the material, statistical fluctuations are not important. For low values of  $T_{\max}^0$  the ceramic presents the same damage almost independently of the distributions, while for high values of  $T_{\max}^0$  the ceramic did not exhibit any damage.
3. Initial defects only affect the cases for which the interface strength,  $T_{\max}$  is in excess of the applied stress amplitude. The velocity histories and crack patterns change depending on the interface parameters. In some cases microcracks do not initiate at the spall plane. The percentage of initial flaws becomes more relevant as the value of  $T_{\max}$  increases.
4. Rate effects eliminate the pullback signal (for relative small values of  $K_{IC}$ ). However, the behavior of the second compressive pulse is similar to the ones found for high values of  $K_{IC}$ . Crack patterns are significantly affected leading to cases where the spall region is defined by a diffused set of isolated microcracks.
5. It was shown that the RVE size is determined by the properties of the ceramic and the amplitude of the stress wave. The lower the amplitude of the applied stress pulse, the larger the RVE needs to be such that all possible values of interface strength and toughness are manifested

within the RVE. The minimum RVE size can be consistently determined using the methodology presented in this work.

## Acknowledgements

The authors acknowledge ARO and DoD HPCMP for providing supercomputer time on the 128 processors Origin 2000 at the Naval Research Laboratory—DC (NRL-DC). This research was supported by the National Science Foundation through Awards no. CMS 9523113 and CMS-9624364 (NSF-CAREER), the Office of Naval Research YIP through Award no. N00014-97-1-0550, the Army Research Office through ARO-MURI Award no. DAAH04-96-1-0331 and the Air Force Office of Scientific Research through Award no. F49620-98-1-0039.

## References

- Ballarini, R., 2000. Personal communication.
- Espinosa, H., 1992. Micromechanics of the Dynamic Response of Ceramics and Ceramic Composites. Ph.D. thesis, Brown University, Providence, RI.
- Espinosa, H., Dwivedi, S., Zavattieri, P., Yuan, G., 1998. Numerical investigations of penetration in multilayered material/structure systems. *Int. J. Solid Struc.* 35 (22), 2975–3001.
- Espinosa, H., Raiser, G., Clifton, R., Ortiz, M., 1992. Experimental observations and numerical modeling of inelasticity in dynamically loaded ceramics. *J. Hard. Mat.* 3, 285–313.
- Evans, A., 1978. Microfracture from thermal expansion anisotropy—(i) single phase systems. *Acta Metall.* 26, 1845–1853.
- Fu, Y., Evans, A., 1985. Some effects of microcracks on the mechanical properties of brittle solids—(i) stress, strain relations. *Acta Metall.* 33, 1515–1523.
- Hearmon, R., 1956. The elastic constants of anisotropic materials ii. *Adv. Phys.* 5, 323–382.
- Lee, Y., Prakash, V., 1999. Dynamic brittle fracture of high strength structural steels under conditions of plane strain. *Int. J. Solids Struct.* 36, 3293–3337.
- Ortiz, M., Suresh, S., 1993. Statistical properties of residual stresses and intergranular fracture in ceramic materials. *J. Appl. Mech.* 60, 77–88.
- Raiser, G., 1993. Dynamic failure resistance of ceramics and glasses. Ph.D. thesis, Brown University, Providence, RI.
- Raiser, G., Clifton, R., Ortiz, M., 1990. A soft-recovery plate impact experiment for studying microcracking in ceramics. *Mech. Mater.* 10, 43–58.

- Raiser, G., Wise, J., Clifton, R., Grady, D., Cox, D., 1994. Plate impact response of ceramics and glasses. *J. Appl. Phys.* 75 (8), 3862–3869.
- Rice, J., 1968. Mathematical analysis in the mechanics of fracture. In: L.H. (Ed.), *Fracture*. Academic Press, New York. pp. 191–311.
- Sridhar, N., Yang, W., Srolovitz, D., Fuller, J.E., 1994. Microstructural mechanics model of anisotropic-thermal-expansion-induced microcracking. *J. Am. Ceram. Soc.* 77 (5), 1123–1138.
- Tvergaard, V., Hutchinson, J., 1988. Microcracking in ceramics induced by thermal expansion or elastic anisotropy. *J. Am. Ceram. Soc.* 71 (3), 157–166.
- Zavattieri, P., Espinosa, H., 2001. Grain level analysis of crack initiation and propagation in brittle materials. *Acta Mater.* 49 (20), 4291–4311.